Doubly heavy tetraquarks from lattice QCD: Incorporating diquark-antidiquark operators and the left-hand cut

Sasa Prelovsek,[1,2,*] Emmanuel Ortiz-Pacheco,[1,3,†] Sara Collins,[4,‡] Luka Leskovec,[1,2,§] M. Padmanath,[5,6,‖] and Ivan Vujmilovic[1,2,¶]

[1]*Jožef Stefan Institute, Jamova 39, 1000, Ljubljana, Slovenia*
[2]*Faculty of Mathematics and Physics, University of Ljubljana, 1000 Ljubljana, Slovenia*
[3]*Department of Physics and Astronomy, Michigan State University, East Lansing, Michigan 48824, USA*
[4]*Institut für Theoretische Physik, Universität Regensburg, 93040 Regensburg, Germany*
[5]*The Institute of Mathematical Sciences, CIT Campus, Chennai, 600113, India*
[6]*Homi Bhabha National Institute, Training School Complex, Anushaktinagar, Mumbai 400094, India*

(Received 11 April 2025; accepted 17 June 2025; published 8 July 2025)

Lattice studies of the doubly charm tetraquark $T_{cc} = cc\bar{u}\,\bar{d}$ require the determination of the DD^* scattering amplitude, which most often incorporate only meson-meson interpolators. We additionally incorporate diquark-antidiquark operators and find that these have some impact on certain eigenenergies. This study presents the first extraction of the DD^* scattering amplitude based on the meson-meson as well as diquark antidiquark interpolators. The effect of the additional operators renders slightly smaller values of $p\,\cot\delta_0$ and a T_{cc} pole slightly closer to the threshold. The scattering amplitude is extracted from eigenenergies by adopting plane-wave and effective-field-theoretic methods, which also incorporate the left-hand cut and address the partial wave mixing. The T_{cc} is found to be a subthreshold resonance with a pole at $m_{T_{cc}} - m_D - m_{D^*} = -5.2^{+0.7}_{-0.8} - i \cdot 6.3^{+2.4}_{-4.8}$ MeV, employing coordinated lattice simulations (CLS) ensembles with $m_\pi \simeq 280$ MeV and the distillation method. A more significant effect of diquark-antidiquark operators on eigen-energies is found for larger heavy quark masses relevant for T_{bb}. We find that deeply bound T_{bb} does not emerge when employing only meson-meson operators, where each meson is separately momentum projected, while the deeply bound state emerges after adding local diquark antidiquark operators.

DOI: 10.1103/rlgp-c9tb

I. INTRODUCTION

The doubly heavy tetraquarks $QQ\bar{u}\,\bar{d}$ with $Q = c, b$ have been the subject of intensive research since the discovery of $T_{cc} = cc\bar{u}\,\bar{d}$ by LHCb Collaboration in 2021 [1,2]. This exotic hadron is a resonance located less than 1 MeV below the $D^{*+}D^0$ threshold and has a narrow decay width to $D^0D^0\pi^+$. It has isospin $I = 0$, while its spin and parity are theoretically expected to be $J^P = 1^+$, although these have not yet been experimentally confirmed. The isospin $I = 1$ counterpart of this channel has been investigated in the lattice quantum chromodynamics (QCD) study [3], where a small negative scattering length and no near-threshold poles in the scattering amplitude have been found, consistent with LHCb results.

This paper investigates $T_{cc} = cc\bar{u}\,\bar{d}$ and explores specific aspects of $T_{bb} = bb\bar{u}\,\bar{d}$, focusing on the $J^P = 1^+$ and $I = 0$ channel in both cases:

T_{cc}: Due to its closeness to the threshold, lattice studies need to determine the DD^* scattering amplitude and extract the mass of T_{cc} from the pole location. So far, most lattice determinations of the DD^* scattering amplitude have incorporated only meson-meson bilocal interpolators $D^{(*)}(\vec{p}_1)D^*(\vec{p}_2)$, where each color-singlet meson is projected to a given momentum [4–8]. One of the aims of this work is to explore the effect of adding localized diquark-antidiquark operators $[cc]_{\bar{3}_c}[\bar{u}\,\bar{d}]_{3_c}$ to the basis. These operators have already been incorporated in [9–12] where the scattering amplitude has not been extracted, as well as in our preliminary proceedings [13] where the scattering amplitude was extracted.

*Contact author: sasa.prelovsek@ijs.si
†Contact author: ortizpac@msu.edu
‡Contact author: sara.collins@ur.de
§Contact author: luka.leskovec@ijs.si
‖Contact author: padmanath@imsc.res.in
¶Contact author: ivan.vujmilovic@ijs.si

All lattice simulations of T_{cc} are performed at larger-than-physical pion masses, where $m_\pi > m_{D^*} - m_D$ holds and the D^* meson is stable. Such kinematics induces a left-hand cut in the partial-wave projected DD^* scattering amplitude, with an associated branch point at real energies immediately below the DD^* threshold, which is a well-known consequence of one-pion exchange in the u channel [14,15]. This invalidates the use of the usual Lüscher's finite-volume formalism [16,17] for extracting the scattering amplitude from lattice eigen-energies along this cut. In this work, this issue is addressed by using an alternative formalism. We adopt an effective potential description of DD^* scattering and solve the Lippmann-Schwinger equation, following Ref. [15]: first in finite volume using the plane-wave basis [18] in order to fit the parameters of the potential to lattice data, and then finally in infinite volume to find the pole in the scattering amplitude.

T_{bb}: This tetraquark has not been experimentally discovered yet, however, a number of reliable theory predictions expect it to be ≈100 MeV below BB^* threshold. Given that it is a bound state well below the threshold, lattice simulations can determine its mass $m = E_1(P = 0)$ most often based on the ground state energy in finite-volume, e.g., [10,19–23]. A variety of interpolators have been employed to extract the ground state energy. Our present study shows that bilocal meson-meson operators $B^{(*)}(\vec{p}_1)B^*(\vec{p}_2)$ alone do not reliably provide the energy in the case of large binding, likely due to small overlap to the localized deeply bound T_{bb}. We find that the inclusion of localized diquark-antidiquark operators significantly affects certain energies; in particular, it shifts the ground state eigenenergy downwards. The bilocal meson-meson operators and diquark-antidiquark operators have already been employed together previously [20,21], however, the energies based solely on bilocal meson-meson operators were not provided.[1]

Our preliminary results incorporating diquark-antidiquark interpolators were presented in [11,13], where the second reference additionally employed the effective field theory (EFT) and plane-wave approach to extract the scattering amplitude.

II. LATTICE SETUP AND HEAVY-LIGHT MESON MASSES

The numerical simulations were performed on two ensembles generated by coordinated lattice simulations (CLS) [24–26] with dynamical u/d and s quarks. They share the same pion mass $m_\pi = 280(3)$ MeV and lattice spacing a, but have different spatial extents as detailed in Table I.

[1]Bilocal operators O^{MM} are called scattering operators in [20,21].

TABLE I. Information on the $N_f = 2 + 1$ CLS lattice ensembles used.

Label	m_π [MeV]	a [fm]	N_L	N_{cfgs}
H105	280(3)	0.08636(98)(40)	32	490
U101			24	255

The light and heavy quarks are based on the relativistic nonperturbatively $O(a)$ improved Wilson-Clover action with the clover term set equal to $c_{sw} = 1.986246$ for all quarks, and different quark masses realized by different hopping parameters κ. Two values of the heavy quark mass are employed: one quark mass is slightly larger than the physical charm quark mass, and the second one, representing the bottom quark, has a smaller-than-physical b-quark mass to avoid too large cutoff effects, which might qualitatively affect the inferences derived here. The employed hopping parameters for light, charm and bottom are $\kappa_{u/d} = 0.13697$, $\kappa_c = 0.12315$ and $\kappa_b = 0.0877$, and the relevant pion and heavy-meson masses are provided in Tables I and II.

The results presented are based on fits to the ensemble average, whereas the uncertainties are determined based on the central 68% distribution of bootstrap samplings. More details on our error analysis are given in Appendix A of [27].

III. OPERATOR BASIS

Finite-volume energies E_n and overlaps Z of the $QQ\bar{u}\,\bar{d}$ system with $Q = c$, b are extracted by evaluating all elements of the correlation matrix

$$C_{ij}(t) = \langle 0|O_i(t+t_i)\mathcal{O}_j^\dagger(t_i)|0\rangle = \sum_{n\geq 1} Z_i^n Z_j^{n*} e^{-E_n t}, \qquad Z_i^n \equiv \langle 0|O_i|n\rangle, \quad (1)$$

and solving the generalized eigenvalue problem (GEVP) [28,29]

$$C(t)\mathbf{u}^{(n)}(t) = \lambda_n(t)C(t_0)\mathbf{u}^{(n)}(t), \qquad \lambda_n(t) \xrightarrow{\text{large } t} A_n e^{-E_n t}. \quad (2)$$

TABLE II. Heavy-light meson masses for two heavy quark masses as determined on the larger volume with $N_L = 32$. The employed b mass is smaller than the physical b-quark mass to avoid too large discretization errors.

$Q = c$	$m_D = 1927(1)$ MeV	$m_{D^*} = 2049(2)$ MeV
$Q = ''b''$	$m_B = 4037(3)$ MeV	$m_{B^*} = 4075(3)$ MeV

Below we present the operators employed to create/annihilate the $QQ\bar{u}\,\bar{d}$ system, where for concreteness $Q = c$, while the same set of operators is used also for $Q = b$. The meson-meson scattering operators resemble DD^* and D^*D^*, where each color-singlet meson is projected to a given momentum $\vec{p}_{1,2}$

$$\mathcal{O}^{MM} = \sum_{\vec{x}_1} e^{i\vec{p}_1\cdot\vec{x}_1}\bar{u}(x_1)\Gamma_1 c(x_1)\sum_{\vec{x}_2} e^{i\vec{p}_2\cdot\vec{x}_2}\bar{d}(x_2)\Gamma_2 c(x_2) - \{\bar{u}\leftrightarrow\bar{d}\}. \tag{3}$$

The corresponding Dirac and color indices are implicitly contracted, and the total momentum is $\vec{P} = \vec{p}_1 + \vec{p}_2$. Such bilocal interpolating fields are most commonly used in lattice scattering studies and have also been employed to investigate the T_{cc} system, see, e.g., [4,5,7–9].

A tetraquark in a diquark-antidiquark configuration can form a color singlet via $(\bar{\mathbf{3}}_\mathbf{c}\otimes\mathbf{3}_\mathbf{c})_{\mathbf{1}_c}$ or $(\mathbf{6}_\mathbf{c}\otimes\bar{\mathbf{6}}_\mathbf{c})_{\mathbf{1}_c}$. The triplet and antitriplet states, $\mathbf{3}_\mathbf{c}$ and $\bar{\mathbf{3}}_\mathbf{c}$, are antisymmetric under color exchange, while the sextet states, $\mathbf{6}_\mathbf{c}$ and $\bar{\mathbf{6}}_\mathbf{c}$, are symmetric. Several studies suggest that the dominant contribution to the energy spectrum comes from the $[cc]_{\bar{3}_c}[\bar{u}\,\bar{d}]_{3_c}$ configuration [30]. We employ local diquark-antidiquark operators where all quarks reside at the same position $\vec{x}$

$$\mathcal{O}^{4q} = \sum_{\vec{x}} \epsilon^{abc}\epsilon^{ade}[c_\alpha^b(\vec{x})\tilde{\Gamma}_1^{\alpha\beta}c_\beta^c(\vec{x})][\bar{u}_\delta^d\tilde{\Gamma}_2^{\delta\sigma}\bar{d}_\sigma^e]e^{i\vec{P}\cdot\vec{x}} \equiv [c\tilde{\Gamma}_1 c][\bar{u}\tilde{\Gamma}_2\bar{d}](\vec{P}). \tag{4}$$

Possible effects of local four-quark operators (4) have not been explored extensively in lattice studies at masses closer to that of the charm quark mass. Their effect on eigenenergies in the T_{cc} channel has been found to be insignificant [9,10] or mild [11–13]. The present paper represents the first study where the effect of diquark antidiquark operators on the extracted DD^* scattering amplitude is explored. Preliminary results of this study, which showed the local four-quark operators may have a mild effect, were presented in our proceedings [13].

With the aim to reliably extract finite-volume energies related to DD^* in partial waves $\ell = 0, 1$, at least up to the lowest inelastic threshold D^*D^*, we incorporate the following interpolating fields with total momenta $|\vec{P}| = 0, 1\cdot\frac{2\pi}{L}$

$T_1^+, \vec{P} = \vec{0}$, row z$(J^P = 1^+, DD^*_{\ell=0,2})$:

$$O_1 = O^{D(0)D^*(0)}_{\ell=0} = \bar{q}\gamma_5 c(\vec{0})\bar{q}\gamma_z c(\vec{0}),$$
$$O_2 = O^{D(0)D^*(0)}_{\ell=0} = \bar{q}\gamma_5\gamma_t c(\vec{0})\bar{q}\gamma_z\gamma_t c(\vec{0}),$$
$$O_3 = O^{D(1)D^*(-1)}_{\ell=0} = \frac{1}{\sqrt{6}}\sum_{\hat{e}_i=\pm\hat{e}_{x,y,z}} \bar{q}\,\gamma_5 c(\hat{e}_i)\bar{q}\gamma_z c(-\hat{e}_i),$$
$$O_4 = O^{D(1)D^*(-1)}_{\ell=2} = \frac{1}{\sqrt{12}}[\bar{q}\gamma_5 c(\hat{e}_x)\bar{q}\gamma_z c(-\hat{e}_x) + \bar{q}\gamma_5 c(-\hat{e}_x)\bar{q}\gamma_z c(\hat{e}_x) + \bar{q}\gamma_5 c(\hat{e}_y)\bar{q}\gamma_z c(-\hat{e}_y) + \bar{q}\gamma_5 c(-\hat{e}_y)\bar{q}\gamma_z c(\hat{e}_y) - 2\bar{q}\gamma_5 c(\hat{e}_z)\bar{q}\gamma_z c(-\hat{e}_z) - 2\bar{q}\gamma_5 c(-\hat{e}_z)\bar{q}\gamma_z c(\hat{e}_z)],$$
$$O_5 = O^{D^*(0)D^*(0)}_{\ell=0} = \bar{q}\gamma_x c(\vec{0})\bar{q}\gamma_y c(\vec{0}),$$
$$O_6 = O^{4q} = [cC\gamma_z c][\bar{u}C\gamma_5\bar{d}](\vec{0}).$$

$A_1^-, \vec{P} = \vec{0}(J^P = 0^-, DD^*_{\ell=1})$:

$$O_1 = O^{D(1)D^*(-1)}_{\ell=1} = \frac{1}{\sqrt{6}}[\bar{q}\gamma_5 c(\hat{e}_x)\bar{q}\gamma_x c(-\hat{e}_x) - \bar{q}\gamma_5 c(-\hat{e}_x)\bar{q}\gamma_x c(\hat{e}_x) + \bar{q}\gamma_5 c(\hat{e}_y)\bar{q}\gamma_y c(-\hat{e}_y) - \bar{q}\gamma_5 c(-\hat{e}_y)\bar{q}\gamma_y c(\hat{e}_y) + \bar{q}\gamma_5 c(\hat{e}_z)\bar{q}\gamma_z c(-\hat{e}_z) - \bar{u}\gamma_5 c(-\hat{e}_z)\bar{q}\gamma_z c(\hat{e}_z)],$$
$$O_2 = O^{D(1)D^*(-1)}_{\ell=1} = O_1(\gamma_5\to\gamma_5\gamma_t, \gamma_i\to\gamma_i\gamma_t),$$
$$O_3 = O^{4q} = [cC\gamma_t c][\bar{u}C\gamma_5\bar{d}](\vec{0}).$$

$A_2, \vec{P} = \frac{2\pi}{L}\hat{e}_z(J^P = 0^-, 1^+, 2^-, DD^*_{\ell=0,1,2})$:

$$O_1 = O^{D(0)D^*(1)} = \bar{q}\gamma_5 c(\vec{0})\bar{q}\gamma_z c(\hat{e}_z),$$
$$O_2 = O^{D(0)D^*(1)} = \bar{q}\gamma_5\gamma_t c(\vec{0})\bar{q}\gamma_z\gamma_t c(\hat{e}_z),$$
$$O_3 = O^{D(1)D^*(0)} = \bar{q}\gamma_5 c(\hat{e}_z)\bar{q}\gamma_z c(\vec{0}),$$
$$O_4 = O^{D(1)D^*(0)} = \bar{q}\gamma_5\gamma_t c(\hat{e}_z)\bar{q}\gamma_z\gamma_t c(\vec{0}),$$
$$O_5 = O^{D^*(1)D^*(0)} = \frac{1}{\sqrt{2}}[\bar{q}\gamma_x c(\hat{e}_z)\bar{q}\gamma_y c(\vec{0}) - \bar{q}\gamma_y c(\hat{e}_z)\bar{q}\gamma_x c(\vec{0})],$$
$$O_6 = O^{4q} = [cC\gamma_z c][\bar{u}C\gamma_5\bar{d}](\hat{e}_z). \tag{5}$$

Light flavors $\bar{q}\,\bar{q}$ in meson-meson operators indicate the isospin 0 combination $\bar{q}\,\bar{q}\to\bar{u}\,\bar{d} - \bar{d}\,\bar{u}$ as in (3).

IV. CORRELATORS WITH MESON-MESON AND LOCAL FOUR-QUARK OPERATORS WITHIN DISTILLATION

We employ the widely used distillation method [31] where all quarks in operators (5) are smeared by applying

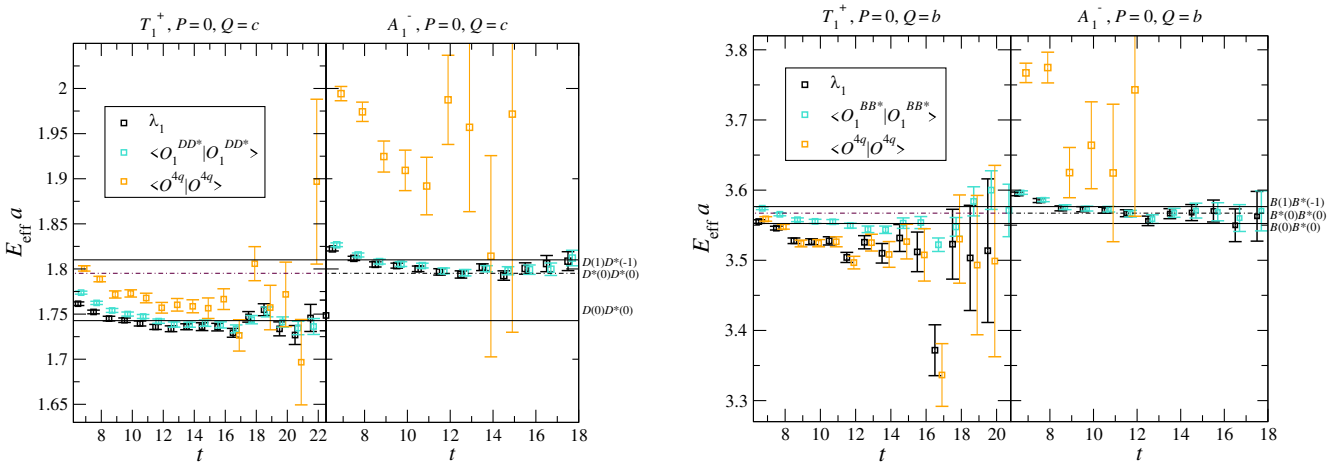

FIG. 1. The effective energies of the diagonal correlators $\langle O^{4q}|O^{4q}\rangle$ and $\langle O^{DD^*}|O^{DD^*}\rangle$ and the GEVP ground state eigenvalue λ_1. Results are shown for two irreducible representations (T_1^+, A_1^-) and two heavy quark masses ($Q=c$, b) on the smaller volume ensemble ($N_L=24$).

the Heaviside Laplacian operator on the pointlike quark fields q_p

$$q^{\alpha c}(\vec{x},t)\equiv\Box_{\vec{x}c,\vec{x}'c'}q_p^{\alpha c'}(\vec{x}',t)=\sum_{k=1}^{N_v}v_{\vec{x}c}^{(k)}(t)v_{\vec{x}'c'}^{(k)*}(t)q_p^{\alpha c'}(\vec{x}',t),$$
$$N_v^{MM}=\begin{cases}60 & (N_L=24)\\ 90 & (N_L=32)\end{cases},\quad N_v^{4q}=\begin{cases}45 & (N_L=24)\\ 55 & (N_L=32)\end{cases}. \tag{6}$$

Our implementation of the Laplacian Heaviside smearing on the quark fields is detailed in [32,33]. The quarks fields in the local four quark operators (4) employ a smaller number of eigenvectors than the meson-meson operators ($N_v^{4q}<N_v^{MM}$) since the computational cost is dominated by the matrix element $\langle O^{4q}|O^{4q\dagger}\rangle$ and rapidly increases with N_v^{4q}. Note that smaller number of eigenvectors corresponds to a wider smearing.

The elements of the correlation matrix (1) are computed from the following three tensors that were precalculated and stored: quark perambulators $\tau^{kk'}$ that correspond to the propagator from eigenvector $v^{k'}$ to eigenvector v^k, rank-2 meson matrices ϕ^{jk} and the rank-4 tetraquark matrices ϕ_{4q}^{jklm}

$$\tau_{\alpha\alpha'}^{kk'}(t,t')=\sum_{\vec{x},c,\vec{x}',c'}v_{\vec{x}c}^{k*}(t)(D^{-1})_{\alpha,\alpha'}^{c,c'}(t,\vec{x};t',\vec{x}')v_{\vec{x}'c'}^{k'}(t'),$$
$$\phi^{jk}(\vec{p},t)=\sum_{\vec{x},c}v_{\vec{x}c}^{j*}(t)v_{\vec{x}c}^{k}(t)e^{i\vec{p}\cdot\vec{x}},$$
$$\phi_{4q}^{jklm}(\vec{P},t)=\sum_{\vec{x},a,b,c,d,e}\epsilon_{abc}\epsilon_{ade}v_{\vec{x}b}^{j}(t)v_{\vec{x}c}^{k}(t)v_{\vec{x}d}^{l*}(t)v_{\vec{x}e}^{m*}(t)e^{i\vec{P}\cdot\vec{x}}, \tag{7}$$

where j, k, l, m represent distillation indices, a, b, c, d, e are color indices and α, α' are Dirac indices. The correlation matrix elements reduce to contractions of τ, ϕ and ϕ_{4q} tensors (7) over their respective indices. The sums over the distillation indices running from 1 to N_v are the most expensive step in the computation. This particularly increases the numerical cost of the calculation of the correlator that involves the tensor ϕ_{4q} since it is of rank 4 in the distillation space, or more precisely

$$\begin{aligned}\langle O^{4q}(t)|O^{4q\dagger}(t')\rangle=&-\phi_{4q}^{jklm}(t,\vec{P})\Gamma_1^{\alpha\beta}\Gamma_2^{\gamma\delta}\\&\cdot[\tau_{\alpha\alpha'}^{jj'}(t,t')\tau_{\beta\beta'}^{kk'}(t,t')\tau_{\gamma\gamma'}^{ll'}(t,t')\tau_{\delta\delta'}^{mm'}(t,t')\\&\Gamma_{1'}^{\alpha'\beta'}\Gamma_{2'}^{\gamma'\delta'}\phi_{4q}^{j'k'l'm'*}(t',\vec{P})\\&-\{j\leftrightarrow k,\alpha\leftrightarrow\beta\}],\end{aligned} \tag{8}$$

where the replacement of indices in the third line applies only within the square parenthesis.

The effective energies of diagonal correlators $\langle O^{4q}|O^{4q\dagger}\rangle$ (8), along with $\langle O^{DD^*}|O^{DD^*\dagger}\rangle$ and the GEVP ground state effective energies are compared in Fig. 1. The correlators based on local four-quark operators show larger errors than those based on meson-meson operators. The local operator O^{4q} in the most relevant irreducible representation T_1^+ leads to a distinctly lower effective mass than that of the bilocal meson-meson operator O_1 in the case of $Q=b$. This is likely related to the important contribution of the diquark-antidiquark Fock component in T_{bb} and the poor overlap of meson-meson scattering operators. The local operator O^{4q} in irrep A_1^- leads to a higher effective mass than the meson-meson operator O_1; this is not surprising since the pseudoscalar diquark $[QC\gamma_t Q]$ is not one of the lower-lying diquarks according to Jaffe's classification in Table III of [30].

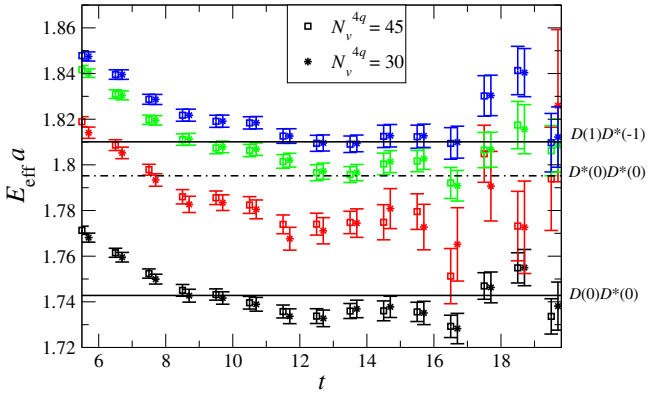

FIG. 2. Effective energies of eigenstates for $\vec{P} = \vec{0}$, irrep T_1^+ on ensemble U101 ($N_L = 24$) employing all six operators. Squares correspond to smearing with $N_v^{4q} = 45$ eigenvectors in O^{4q}, while stars correspond to $N_v^{4q} = 30$. In both cases, $N_v^{MM} = 60$ is employed. Note that all other results and figures employ the N_v given in (6).

We note that the correlators (8) involving the local four-quark operators with $N_v^{4q} \simeq 50$ turned out to be at least an order of magnitude more costly in our implementation than the correlators employing just meson-meson operators with $N_v^{MM} \simeq 100$. A recent proceedings [12] proposes a different method that is also based on the precalculated perambulators τ, but avoids tensors of rank-4 in the distillation space [12].

V. FINITE-VOLUME ENERGIES, OVERLAPS, AND IMPACT OF LOCAL FOUR-QUARK OPERATORS

This section presents the energies E_n of the finite-volume eigenstates and their overlaps to operators $Z_i^n = \langle O_i|n\rangle$, and details the investigation of the impact of local-four quark operators. All results are obtained employing the GEVP (2) with $t_0 = 4$, using correlators which are averaged over 5 or 8 source time slices t_i (1), over three polarizations (for T_1^+) or three total momenta (for $|\vec{P}| = 2\pi/L$).

A comparison of the results for two different smearing widths for the quarks in operators O^{4q} in Fig. 2 indicates that errors on certain effective energies decrease slightly when going from a larger width ($N_v^{4q} = 30$) to a smaller width ($N_v^{4q} = 45$). This affects the errors on eigenstates that couple to the local four-quark operators.

In the following, we present lattice energies as $E_n = \Delta E_n^{lat} + E_{con}^{ni}$ which will represent an input to the scattering analysis. Here, the energy shifts ΔE_n^{lat} and the continuum noninteracting energies E_{con}^{ni} are

$$\Delta E_n^{lat} = E_n^{lat} - E^{lat}_{D^{(*)}(\vec{p}_1)} - E^{lat}_{D^*(\vec{p}_2)}$$
$$E_{con}^{ni} = (m^2_{D^{(*)}} + \vec{p}_1^{\,2})^{1/2} + (m^2_{D^*} + \overrightarrow{p_2}^2)^{1/2}. \quad (9)$$

The combination $\Delta E_n^{lat} + E_{con}^{ni}$ mitigates small deviations of single-hadron energies from their continuum values and ensures that the scattering amplitude is zero if ΔE_n^{lat} is zero.

Below we discuss the spectrum and overlaps separately for the two heavy-quark masses employed, as certain findings are quite different:

(i) $Q = c$: The spectrum for the charm sector in Fig. 3(a) compares eigenenergies obtained including meson-meson and diquark-antidiquark operators (violet), eigenenergies obtained including only meson-meson operators (blue) and noninteracting energies $E^{ni} = E_{D^{(*)}}(\vec{p}_1) + E_{D^*}(\vec{p}_2)$ (lines). The energies remain roughly unaffected by the inclusion of diquark-antidiquark operators, i.e., the energies employing basis $D^{(*)}D^*$ and $D^{(*)}D^* + [cc][\bar{u}\,\bar{d}]$ are consistent within the 1σ statistical uncertainties. The exception is the second eigenstate in irreducible representation T_1^+, whose energy is decreased by a few σ with the inclusion of diquark antidiquark operators, as confirmed also in Fig. 4 that scrutinizes various fit-ranges for this level. The normalized overlaps of eigenstates to employed operators are presented in Fig. 3(b). The diquark-antidiquark operator couples to several eigenstates, which is expected as it has the same quantum numbers and is Fierz-related to other interpolators used [34,35]. The pattern of overlaps $\langle n|O^{MM}\rangle$ remains mostly unaffected with the inclusion of diquark-antidiquark operators. In particular, each level is dominantly coupled to only one of the DD^* or D^*D^* operators (in addition to being possibly coupled also to the diquark-antidiquark operator), which is advantageous for the one-channel DD^* scattering analysis performed below.[2]

(ii) $Q =$ "b": The BB^* and B^*B^* thresholds lie much closer together due to the hyperfine splitting decreasing with increasing heavy quark mass. The influence of local four-quark operators is striking for this heavy quark mass. This is evidenced by the spectrum in Fig. 5(a), where the pattern of eigenenergies is affected when including the local $[bb][\bar{u}\,\bar{d}]$ operator (violet) in addition to the bilocal operators $B^{(*)}(\vec{p}_1)B^*(\vec{p}_2)$ (blue). The most prominent effect with the inclusion of local four-quark operators in the basis is the observation of a new distinct ground state in the T_1^+ and A_2 irreps that were inaccessible with purely bilocal meson-meson interpolators.

The large statistically significant difference between the ground state energies using a basis with or without the local four-quark operators is evident from the $t_{\rm min}$ dependence of energy splittings

[2]The exception to the last two sentences is level $n = 3$ in T_1^+ on the $N_L = 24$ ensemble, which lies very near the D^*D^* threshold and is therefore not included in the scattering analysis below.

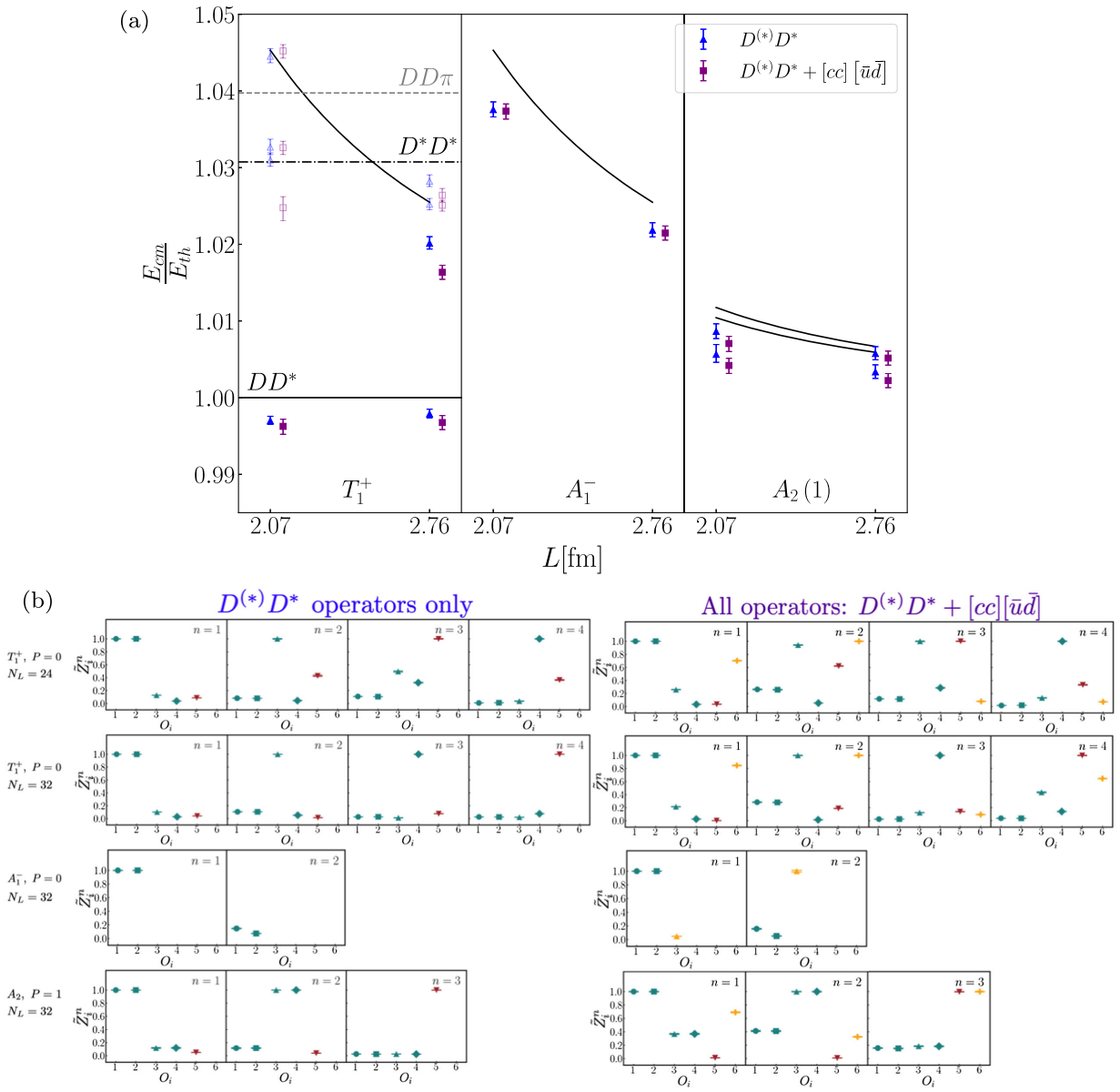

FIG. 3. (a) Finite-volume energy spectrum for $Q = c$, shown in the form of the ratio E_{cm}/E_{th} with $E_{th} = m_D + m_{D^*}$: results including all interpolators (violet), results including only meson-meson interpolators and excluding local four quark operators (blue) and the noninteracting energies (lines) are displayed. The filled symbols indicate energy levels employed in the scattering analysis. (b) The normalized overlaps of eigenstates to employed operators: here $Z_i^n = \langle n|O_i\rangle$, while $\tilde{Z}_i^n \equiv Z_i^n/\max_{n'} Z_i^{n'}$ is normalized by the overlap of the operator O_i to the state that has largest overlap to this operator among all eigenstates. Therefore $\tilde{Z}$ is independent of the normalization of the operator.

presented in Fig. 6. The ground state from the basis omitting local four-quark operators and the first excited state from the basis including them have nearly consistent energies. This corroborates the idea that the ground state observed using the enlarged basis represents a new distinct level.

The operator-state overlaps in Fig. 5(b) also show prominent effects with the inclusion of the diquark-antidiquark operators, supporting the statement above. The ground states in irreps T_1^+ and A_2 are dominantly coupled to diquark-antidiquark operators, and show no characteristic resemblance to the pattern of overlaps for any levels determined using purely bilocal meson-meson interpolators [see Fig. 5 (b)]. This is in line with the expectation that the local diquark-antidiquark Fock component plays a dominant role in T_{bb} according to many lattice and phenomenological studies, e.g., [10,19–23,36–39]. The overlap factors in the first excited state in the T_1^+ irrep from the enlarged basis can be approximately

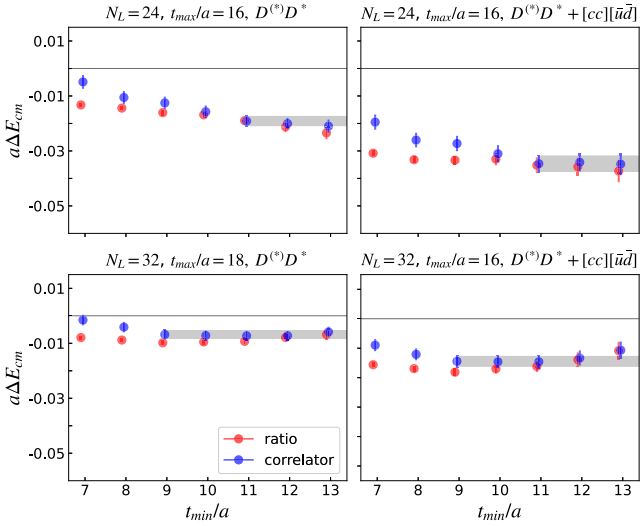

FIG. 4. Energy shifts (9) of the first excited eigenenergy in the T_1^+ irrep in the charm sector that is affected by the inclusion of O^{4q}: $\Delta E = E_2 - E_{D(1)} - E_{D^*(1)}$. Results using only meson-meson operators (left) and using all interpolators (right) are shown. The shifts are displayed as a function of the t_{min} utilized in the one-exponential fit. The gray bands indicate the chosen fit estimates employed in the scattering analysis. They are evaluated using energy estimates from separate fits to each of the correlators involved. The label "ratio" refers to energy splittings extracted from single fits to the ratio of the interacting eigenvalue correlators to the product of single meson correlators, whereas the label "correlator" refers to the same quantity extracted from separate fits to each of the correlators involved. Other levels are not significantly affected by the inclusion of O^{4q} for $Q = c$.

seen to reflect the patterns for the ground state using purely meson-meson interpolators. Such a comparison of overlaps for higher levels and the levels in the A_2 irrep is more complicated as the inclusion of local four-quark operators leads to eigenstates with comparable couplings to both meson-meson operators of type BB^* and B^*B^*.

The observation of this lower level with the enlarged basis indicates that bilocal meson-meson interpolators fail to access the ground state in the T_{bb} sector within moderate physical time separations. With the inclusion of the local diquark-antidiquark operator, we obtain a T_{bb} binding energy of approximately 60 ± 10 MeV for the lighter-than-physical b quark we investigate (see Table II). The deep binding of T_{bb} was reported by previous lattice studies [20,21] that used local diquark-antidiquark operators alongside local and bilocal meson-meson interpolators in their analysis. These two studies employed nonrelativistic QCD for bottom quarks, while our present study confirms this finding with relativistic bottom quarks. Several other studies also have reported similar deep binding using only local $BB^* = (b\bar{d})(b\bar{u})$ operators together with local diquark-antidiquark interpolators [10,19,22,40,41].[3] The only previous lattice simulation of T_{bb} that evaluates all correlators between bi-local $B(0)B^*(0)$ and local $[bb][\bar{u}\,\bar{d}]$ did not present the result based on bilocal $B(0)B^*(0)$ operators alone [21]. In addition to the heavy-quark treatment mentioned above, there are further differences between Ref. [21] and our study: the former employed stochastic noise propagators for evaluating Wick contractions and we employ distillation method; the former is based on the staggered action for light quarks and we use Wilson-clover action.

The finite-volume energies in the bottom sector presented in Fig. 5(a) have significant statistical errors and are also expected to have significant heavy-quark discretization errors. They are not, therefore, reliable enough to be utilized to extract the scattering amplitudes. In addition, the closeness of the BB^* and B^*B^* thresholds calls for the extraction of the coupled-channel scattering matrix for both channels, which is beyond the scope of the present study.

VI. DD^* SCATTERING AMPLITUDE FROM EFFECTIVE FIELD THEORY AND PLANE-WAVE APPROACH

We aim to determine the DD^* scattering amplitude T_l for the lowest partial waves $l = 0, 1$. These amplitudes can be expressed in terms of the scattering phase shift δ_l as [14]

$$-\frac{2\pi}{m_r} T_l^{-1} = p \cot \delta_l - ip, \tag{10}$$

where m_r is the reduced mass of the DD^* system. The main obstacle to the applicability of Lüscher's formalism for extracting scattering amplitude is the existence of a left-hand cut. This results from the one-pion exchange (OPE), illustrated on the right-hand side of Fig. 7(b), when the pion comes on-shell [14]. For this reason, we will employ an effective field theory approach, where the DD^* potential V is represented by the sum of the one-pion exchange and the local DD^* interaction. The unknown local interaction will be parametrized using several free low-energy constants. These constants are determined by fitting the lattice spectrum to the energies of Hamiltonian $H = \frac{p^2}{2m_r} + V$ in the finite volume and in the plane wave basis, introduced in [18]. Once the parameters of the potential are known, the scattering amplitude T is determined from the Lippmann-Schwinger equation illustrated in Fig. 7(a) in infinite

[3]Lattice investigations following static potential-based and HALQCD-potential based approaches also predict similar binding energies in T_{bb} system [36,37,42].

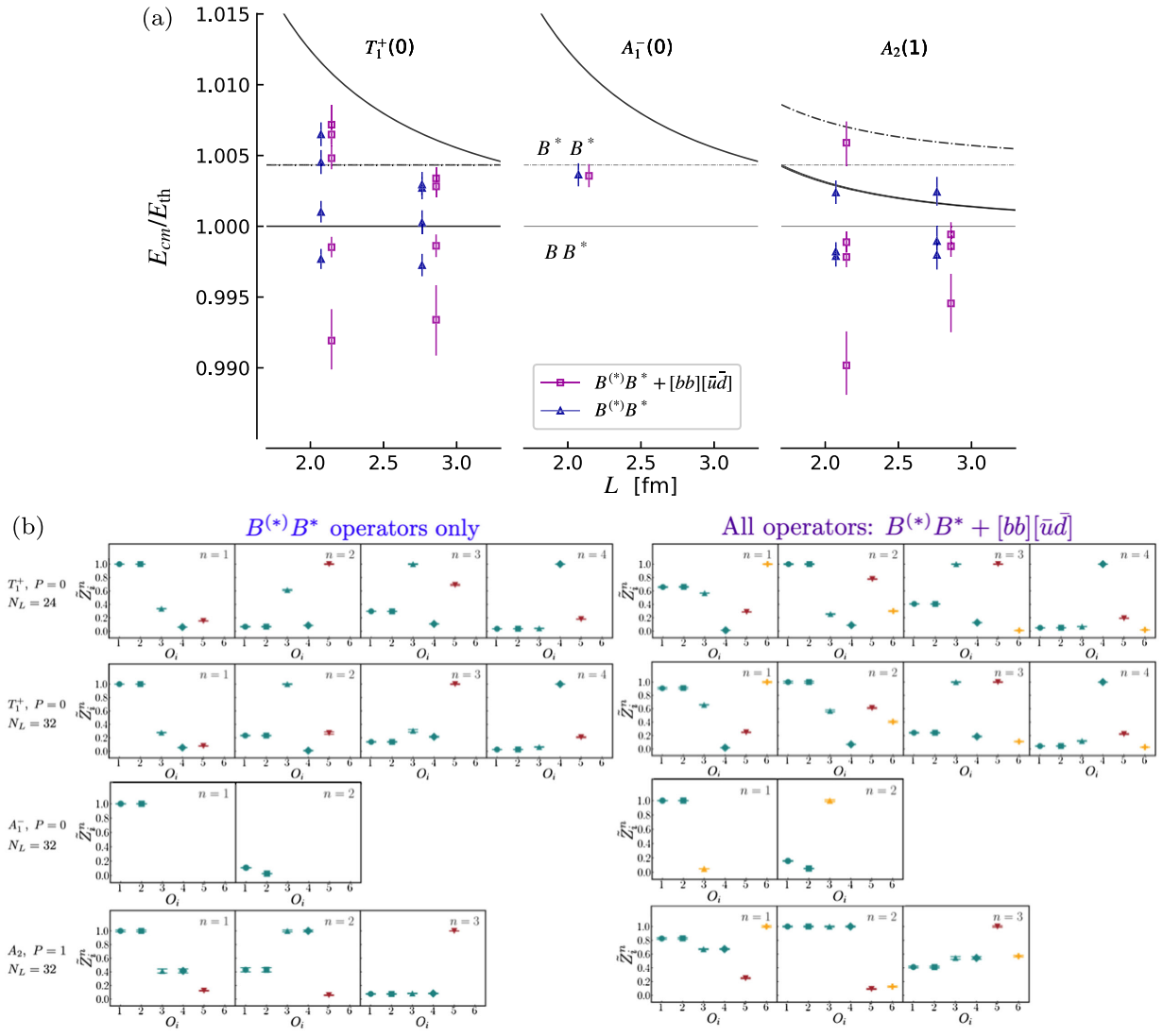

FIG. 5. (a) Finite-volume energy spectrum E_{cm}/E_{th} with $E_{th} = m_B + m_{B^*}$ for $Q = b$: results including all interpolators (violet), results including only meson-meson interpolators and excluding local four quark operators (blue) and noninteracting energies (lines). The irrep A_1^- has not been simulated on a larger volume to reduce the cost of simulation. (b) Corresponding normalized overlaps $\tilde{Z}_i^n \equiv Z_i^n / \max_{n'} Z_i^{n'}$.

volume. The kinematics of D and D^* mesons are treated in the nonrelativistic limit as in Sec. 5 of [18] since we consider the scattering amplitude at energies in the close vicinity of the DD^* threshold.

A. The Lippmann-Schwinger equation

The scattering amplitude T and DD^* potential V are related via the Lippmann-Schwinger equation (LSE) illustrated in Fig. 7(a) for the center-of-momentum (CMF) frame[4]

$$T = V - V\mathcal{G}T,$$
$$T(\vec{p},\vec{p}';E) = V(\vec{p},\vec{p}') - \int \frac{d\vec{k}}{(2\pi)^3} V(\vec{p},\vec{k}) G(\vec{k};E) T(\vec{k},\vec{p}';E). \tag{11}$$

The second relation corresponds to the infinite volume, while the first relation can be conveniently expressed in terms of matrices for a finite basis in the finite volume. Our main aim is to extract the infinite-volume on-shell scattering amplitude $T(|\vec{p}| = |\vec{p}'| = p;\ E \simeq E_{th} + p^2/2m_r)$, while the off-shell amplitude inherently appears within the integrand. Here G is the propagator which reduces to the Green's function of the Schrödinger equation in the

[4]The sign of G differs from [13,18] and is consistent with [7,14].

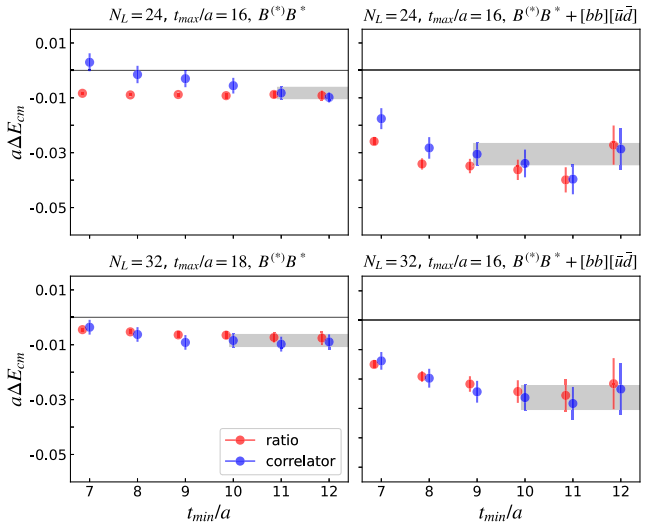

FIG. 6. Energy shift (9) for one of the levels that are significantly affected with the inclusion of O^{4q} in the "bottom" sector: $\Delta E = E_1 - m_B - m_{B^*}$ for the ground state in irrep T_1^+ as a function of $t_{\min}$ in the one-exponential fit. A number of other levels are also significantly affected by the inclusion of O^{4q} for $Q = b$, as evidenced in Fig. 5. The definitions of red, blue, and gray shifts are detailed in the caption of Fig. 4.

nonrelativistic limit [see footnote quoted before Eq. (11)]

$$G(p^0, \vec{p}) = \frac{1}{\frac{\vec{p}^2}{2m_r} - p^0 + i\epsilon}, \tag{12}$$

and is placed in the plane-wave basis through

$$\mathcal{G} = \frac{\Delta\vec{k}}{(2\pi)^3} G = \frac{1}{L^3} G. \tag{13}$$

Poles of the scattering amplitude T (11)

$$T = (\mathcal{G}^{-1} + V)^{-1} \mathcal{G}^{-1} V \tag{14}$$

are determined from

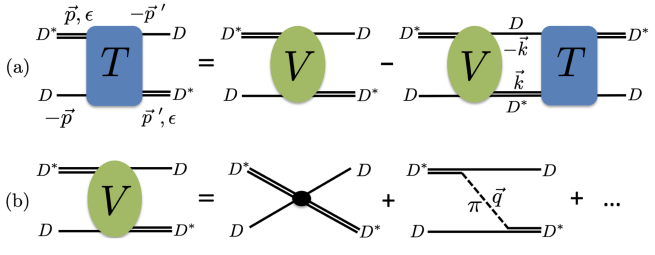

FIG. 7. (a) Lippmann-Schwinger relation between scattering amplitude T and potential V, where momenta refer to the center-of-momentum frame. (b) Effective potential V defined in (22) (Note that signs of the momenta differ with respect to [7]).

$$\det(\mathcal{G}^{-1} + V) = 0, \tag{15}$$

which in turn leads to the familiar Hamiltonian equation when the propagator G defined in (13) is inserted into the determinant equation

$$\det(H - p^0 I) = 0, \qquad H = \frac{p^2}{2m_r} I + \frac{1}{L^3} V. \tag{16}$$

Note that the units of the potential V and scattering amplitude T are $1/\mathrm{GeV}^2$, which renders the correct units (GeV) for the Hamiltonian. The same relation also holds in finite volume where it is projected to appropriate irreducible representations Γ of the octahedral group O_h or one of its little groups

$$\det(H^\Gamma - p^{0,\Gamma} I) = 0. \tag{17}$$

This equation is fulfilled precisely when $p^{0,\Gamma}$ equals one of the finite-volume energies E_n^{cm} on the lattice. This relation is used to extract the free parameters of the potential by fitting to lattice eigenenergies. This approach has been introduced for the two-nucleon case in Sec. 5 of [18].

B. The effective potential

The application of the Lippmann-Schwinger equation necessitates the use of an effective potential when parametrizing the interaction in the DD^* system. This will be composed of a one-pion exchange and a contact DD^* interaction

$$V = V_\pi + V_{CT}. \tag{18}$$

The one-pion exchange is incorporated via the effective Lagrangian [43]

$$\mathcal{L}_{\text{int}} = \frac{g}{2f_\pi}(D^{*\dagger} \cdot \nabla \pi^a \tau^a D + \text{H.c.}),$$
$$\pi^a \tau^a = \begin{pmatrix} \pi^0 & \sqrt{2}\pi^+ \\ \sqrt{2}\pi^- & -\pi^0 \end{pmatrix}. \tag{19}$$

While the physical values of the low-energy constants from (19) are $g^{ph} \simeq 0.57$ and $f_\pi^{ph} = 92.2$ MeV, we take their values at $m_\pi \simeq 280$ MeV: $g = 0.645$ is based on the lattice simulation [44] and $f_\pi = 105$ MeV is based on chiral perturbation theory (see Appendix A 3 in [14]). The potential between DD^* mesons is then given as

$$V_\pi(\vec{p}, \vec{p}\,') = 3\left(\frac{g}{2f_\pi}\right)^2 \frac{(\vec{\epsilon}\cdot\vec{q})(\vec{\epsilon}\,'^*\cdot\vec{q})}{q^2 - m_\pi^2}, \tag{20}$$

with momentum transfer $\vec{q} = \vec{p} + \vec{p}\,'$. The s-wave projection of the potential, derived in [7], features a left-hand cut beginning approximately at $p_{lhc}^2 \approx -\mu_\pi^2/4 \simeq -10^{-3} E_{th}^2$ with

$\mu_\pi^2 \equiv m_\pi^2 - (m_{D^*} - m_D)^2 > 0$ for our DD^* system. This is the energy below which the exchanged pion can come on shell, and the cut extends to $-\infty$ along the real energy. The central part of the potential V_π in (20) contributes to the attraction at short distances and slight Yukawa-like repulsion at long distances as elaborated in [7]

$$V_\pi^{\rm cent}(\vec{q}) = \left(\frac{g_c}{2f_\pi}\right)^2 \frac{\vec{q}^2}{q^2 - m_\pi^2} = \frac{g_c^2}{4f_\pi^2}\left(-1 + \frac{\mu_\pi^2}{\vec{q}^2 + \mu_\pi^2}\right),$$
$$V_\pi^{\rm cent}(r) = \frac{g_c^2}{4f_\pi^2}\left(-\delta^{(3)}(\vec{r}) + \frac{\mu_\pi^2}{4\pi r} e^{-\mu_\pi r}\right), \quad (21)$$

which will be important for the interpretation of our results.

The contact potential V_{CT} near the threshold is parametrized via a low-energy expansion with the two lowest terms for $l = 0$, and one term for $l = 1$ as in [15]. The employed potential for DD^* system in Fig. 7(b) with CMF momenta $\vec{p}$ and $\vec{p}'$ is then

$$V(\vec{p},\vec{\epsilon};\vec{p}',\vec{\epsilon}') = \Big[(2c_0^s + 2c_2^s(\vec{p}^2 + \vec{p}'^2))(\vec{\epsilon}\cdot\vec{\epsilon}'^*) + 2c_2^p(\vec{p}\cdot\vec{\epsilon})(\vec{p}'\cdot\vec{\epsilon}'^*) + 3\left(\frac{g}{2f_\pi}\right)^2 \frac{(\vec{\epsilon}\cdot\vec{q})(\vec{\epsilon}'^*\cdot\vec{q})}{q^2 - m_\pi^2}\Big] \cdot f_{\rm reg}, \quad (22)$$

which is illustrated in Fig. 7(b). The last term accounts for the left-hand cut and incorporates it in our search for the pole of the scattering amplitude. Additionally, three low-energy constants (LECs) are introduced: $c_{0,2}^s$ for s-wave and c_2^p for p-wave.

The function

$$f_{\rm reg}(|\vec{p}|,|\vec{p}'|) = \exp\left(-\frac{|\vec{p}|^n + |\vec{p}'|^n}{\Lambda^n}\right) \quad (23)$$

regularizes the potential, and our main result is based on a rather sharp cutoff with $n = 40$ and $\Lambda = 0.65$ GeV set near the D^*D^* threshold, slightly above the energy of $D(1)D^*(-1)$ on our smaller volume. Our main conclusions remain robust with the choices $n = 10$–40 and $\Lambda = 0.5$–0.65 GeV considered in the Appendix, while increasing Λ further is not appropriate due to the omission of the D^*D^* channel in the scattering analysis.

C. Hamiltonian in the plane wave basis

The natural choice of basis for the matrices in the Lippmann-Schwinger equation is composed of plane waves, which in the laboratory and center-of-momentum frames take on the following forms, respectively:

$$|D(\vec{p}_D); D^*(\vec{p}_{D^*},\vec{\epsilon}^r)\rangle_{lat}, \qquad \vec{P} = \vec{p}_D + \vec{p}_{D^*},$$
$$\vec{p}_{D^{(*)}} = \frac{2\pi}{L}\vec{n}_{D^{(*)}}, \vec{n}_{D^{(*)}} \in Z^3; \qquad r = x,y,z, \quad (24)$$

and

$$|D(\vec{k}); D^*(-\vec{k},\vec{\epsilon}^r)\rangle_{cm}. \quad (25)$$

Our aim now is to evaluate the Hamiltonian H in the plane wave basis and transform it to irreducible representation H^Γ, where an example of this is explicitly shown in Appendix B. The plane-wave basis is finite due to the cutoff of the effective field theory, which is implemented in the potential via the regularization function $f_{\rm reg}$. The expression (22) for the potential V applies in the CMF, therefore one forms the basis (25), which is obtained by a Lorentz transformation from the lattice frame to CMF.[5] The Hamiltonian matrix in plane wave basis is composed of matrix elements

$$H_{\vec{k}r,\vec{k}'r'} = \langle D(\vec{k}); D^*(-\vec{k},\vec{\epsilon}^r)|H|D(\vec{k}'); D^*(-\vec{k}',\vec{\epsilon}^{r'})\rangle, \quad (26)$$

with H and V defined in (16) and (22), respectively. The final step is applying a unitary transformation U^Γ, which converts the total plane-wave basis (24) into a basis that transforms irreducibly with respect to the lattice symmetry group, where the irreducible representations are set to $\Gamma = T_1^+, A_1^-, A_2$. The resulting basis resembles the DD^* operators in (5), and the projection technique to get this basis is well-established and explained in, e.g., [18,45]. The Hamiltonian matrix H^Γ in the irreducible basis Γ then equals $H^\Gamma = U^\Gamma H U^{\Gamma\dagger}$. Its energy spectrum (i.e., the eigenvalues of H^Γ) is afterward fitted to the observed lattice eigenenergies E^{cm} obtained from the principal correlators $\lambda_n(t)$ shown in (2).

VII. RESULTS ON DD^* SCATTERING

This section provides results for the DD^* potential, on-shell scattering amplitude, and the location of the T_{cc} pole obtained from the lattice energies, following the formalism described in the previous section.

A. Potential and its low-energy constants

The potential V (22) incorporates s-wave and p-wave interactions, and depends on three unknown low-energy constants c_0^s, c_2^s and c_2^p. These are determined from the fit to the lattice eigen-energies. In particular, the eigenenergies of the effective Hamiltonian H (16) based on this potential and plane-wave basis are fitted to the lattice energies E_{cm} indicated by filled symbols in Fig. 3. The resulting fits are shown in Fig. 8 and Table III for the simulations including

[5]This Lorentz transformation does not modify polarization ϵ^r in the nonrelativistic limit.

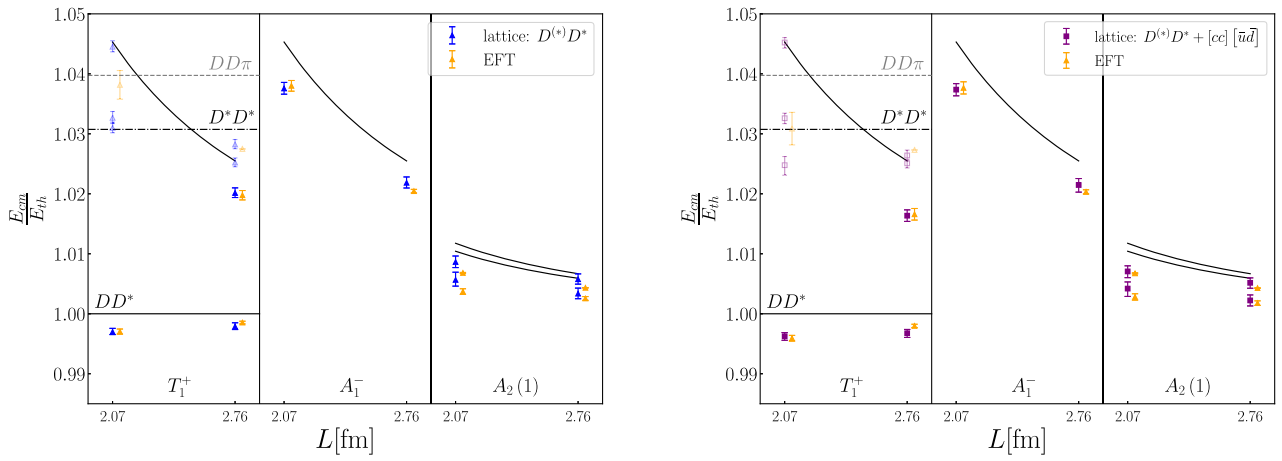

FIG. 8. Fit of the low-energy constants parameterizing the potential: blue and violet points represent energies obtained from the lattice, while orange points are reconstructed from the fitted effective potential (17). The lattice data on the right incorporates the diquark-antidiquark interpolator, while the lattice data on the left omits it. The fit is based on the cutoff parameters $\Lambda = 0.65$ GeV and $n = 40$ (23).

and excluding diquark-antidiquark operators. The reproduction of the lattice energies is particularly favorable for the data incorporating $[cc][\bar{u}\,\bar{d}]$ interpolators ($\chi^2/n_{\rm dof} = 1.4$), while also the fit omitting these operators is acceptable ($\chi^2/n_{\rm dof} = 2.4$). The inclusion of diquark-antidiquark operators mainly decreases the slope coefficient c_2^s, while the other two parameters remain unmodified. These results are based on the preferred choice of a rather sharp cutoff $\Lambda \simeq 0.65$ GeV set near the D^*D^* threshold with $n = 40$ in (23). Choices $\Lambda = 0.5$ GeV, 0.65 GeV and $n = 10$–40 lead to somewhat less favorable fits, while the main conclusions remain, as detailed in Appendix A.

B. Scattering amplitudes in EFT plane-wave approach and Lüscher's approach

Once the low-energy constants and, therefore, the potential is fixed, the same potential is used in the infinite-volume Lippmann-Schwinger equation (11) to determine the scattering amplitude. The scattering amplitude is related to the scattering phase shift via (10) and the resulting $p\cot\delta_0$ for s-wave is shown in Fig. 9. The values of $p\cot\delta_0$ near the threshold obtained with and without diquark-antidiquark operators are roughly similar: the inclusion of the diquark-antidiquark operators shifts the value down by about $1-1.5\sigma$, which brings it closer to the crossing with the $ip = \pm|p|$ curve shown in red. The inclusion of these operators also decreases the slope of $p\cot\delta_0$ above the threshold, leading to smaller values of $p\cot\delta_0$ and, therefore, a more attractive interaction. Note that this $s-$wave scattering result is obtained from lattice energies using a fit that incorporates $s-$ as well as $p-$wave interactions between D and D^*.

The same Fig. 9 also shows the values of $p\cot\delta_0$ based on Lüscher's method, where the black circles are obtained from individual energy levels assuming a negligible $p-$wave interaction. In line with expectations, both methods are in good agreement at energies above the left-hand cut, marked with a vertical green line. The two approaches are not expected to agree in the vicinity of or below the left-hand cut since the EFT incorporates this cut while Lüscher's approach omits it.

TABLE III. The low-energy constants appearing in the DD^* potential (22) and χ^2 from the fit of lattice eigenenergies based on EFT with cutoff $\Lambda = 0.65$ GeV and $n = 40$ (23). The E^p represents the location of the pole of the resulting DD^* scattering amplitude on the second Riemann sheet.

	Operators $D^{(*)}D^*$	Operators $D^{(*)}D^* + [cc][\bar{u}\,\bar{d}]$
c_0^s[GeV^{-2}]	-3.5 ± 1.0	-3.6 ± 1.0
c_2^s[GeV^{-4}]	6.6 ± 2.9	1.3 ± 2.9
c_2^p[GeV^{-4}]	10.1 ± 1.0	9.8 ± 1.1
χ^2/dof	2.4	1.4
$E^p - E_{th}$ [MeV]	$-8.5^{+1.8}_{-2.4} \pm i \cdot 10.3^{+3.2}_{-4.1}$	$-5.2^{+0.7}_{-0.8} \pm i \cdot 6.3^{+2.4}_{-4.8}$
$E_{lhc} - E_{th}$ [MeV]	$-7.98(5)$	$-7.98(5)$
$(p_{lhc}/E_{th})^2 \times 10^4$	$-10.03(8)$	$-10.03(8)$

C. T_{cc}^+ pole

In order to search for poles, the scattering amplitude is continued to the complex energy plane and Riemann sheets I and II are explored.[6] The corresponding on-shell scattering amplitude T_I for complex p and $E = E_{th} + p^2/2m_r$ is a solution of Lippmann-Schwinger equation (11), where the integral runs over the real momenta $d\vec{k}$. The amplitude on

[6]Riemann sheet I corresponds to $\mathrm{Im}(p) > 0$, while II corresponds to $\mathrm{Im}(p) < 0$.

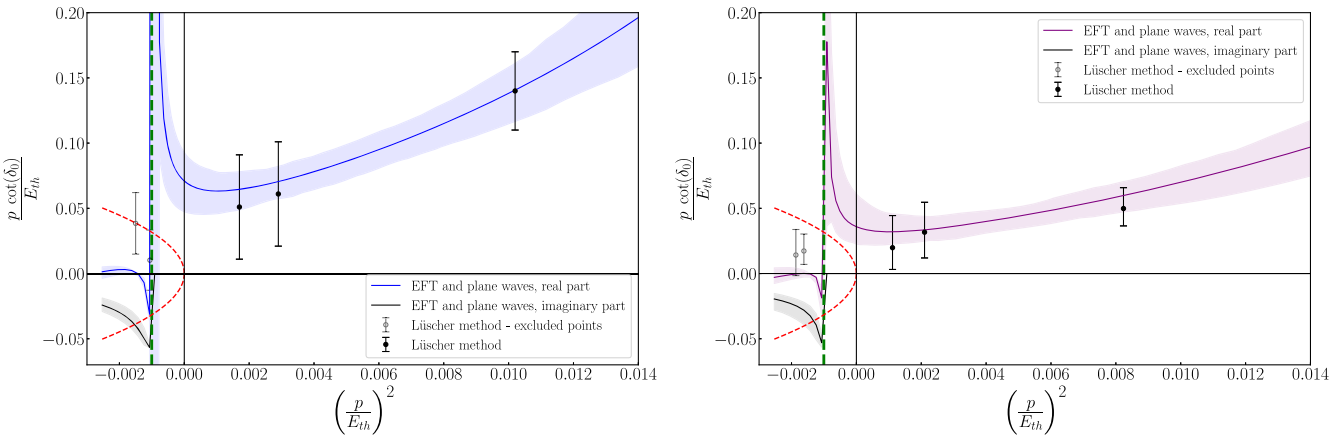

FIG. 9. Comparison of s-wave DD^* scattering phase shifts shown in terms of $p\cot\delta_0$ normalized to E_{th}: the left plot features only meson-meson data, while the analysis displayed in the right plot also incorporates a diquark-antidiquark interpolator. The blue and violet bands represent $\mathrm{Re}(p\cot\delta_0)$ based on the EFT approach with s and p waves, while the full and empty black circles are based on Lüscher's method assuming negligible $p-$wave. The vertical green line marks the beginning of the left-hand cut, below which the EFT also renders an imaginary part of $p\cot\delta_0$ shown in gray. The red line represents $ip = \pm|p|$.

the second sheet is obtained via $T_{II}^{-1} = T_I^{-1} - 2i\frac{m_r}{2\pi}\sqrt{2m_rE}$ in order to satisfy $S_{II}(E) = S_I^{-1}(E)$.[7]

The pole location of T_{cc}^+ is presented in Fig. 10 and Table III. This result is based on our full operator basis and the pole appears as a subthreshold resonance on the second Riemman sheet.

The comparison of pole T_{cc}^+ locations for the operator basis, including and excluding diquark-antidiquark operators, is shown in Fig. 11 and Table III. In both cases, the tetraquark appears as a subthreshold resonance, which corresponds to a pole on the second Riemann sheet that lies less than 10 MeV below the DD^* threshold. The data that incorporates the diquark-antidiquark interpolator shows somewhat greater attraction in the system. The inclusion of this operator shifts the pole slightly closer to the threshold and the physical scattering axis where the pole would turn to a virtual state pole. This is consistent with the $p\cot\delta_0$ curve approaching $ip = |p|$ in Fig. 9; the crossing of $p\cot\delta_0$ and $ip = -|p|$ would imply a virtual state pole at real energy below the threshold.

D. Discussion

Our lattice simulation considers DD^* scattering in a kinematical situation where D^* is stable since $m_\pi \simeq 280$ MeV $> m_{D^*} - m_D$. The attraction in the DD^* system and thereby the presence of the pole follows from the attractive DD^* potential at short distance, represented by the negative contact term c_0 (22) and negative term in the one-pion exchange (21). Focusing on $s-$wave interaction, the fully attractive potential would have rendered a virtual or a bound state pole on the real energy axes. However, the DD^* scattering at lattice kinematics with $m_\pi > m_{D^*} - m_D$ receives a contribution from one-pion exchange (21) that renders also a slightly repulsive Yukawa-like part at longer distances. This slightly repulsive part is responsible for T_{cc} featuring as a subthreshold resonance at physical charm quark mass and our m_π.

One anticipates that with decreasing m_π and/or increasing heavy quark mass, the T_{cc} resonance pole will transition to the virtual-state pole and then to the bound state pole, as elaborated in [7,46,47] based on the existing lattice simulations.

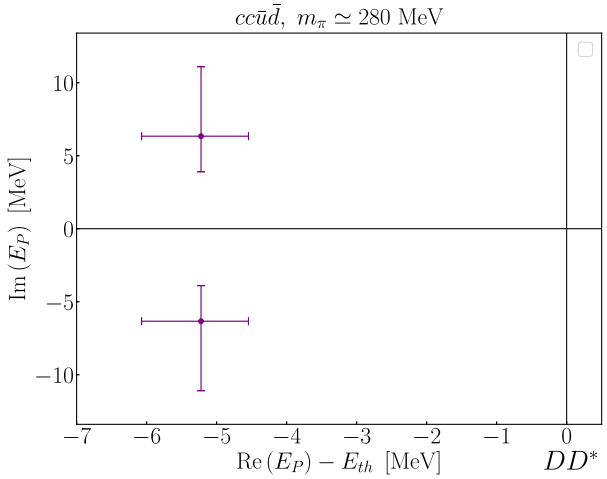

FIG. 10. The resulting location of the T_{cc}^+ pole in DD^* scattering amplitude at the employed $m_\pi \simeq 280$ MeV. The pole appears on the second Riemann sheet, and the origin represents the DD^* threshold. This result is based on the full operator basis.

[7]Here $S_{II} = 1–2i\frac{m_r}{2\pi}p_{II}T_{II}$ and the square-root function has a cut on the positive real axes with $\mathrm{Im(E)} \geq 0$.

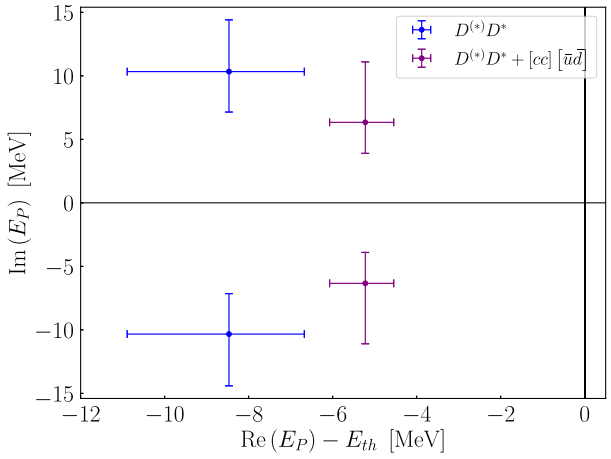

FIG. 11. The locations of the T_{cc}^{+} poles in DD^* scattering amplitude, shown also in Table III. The violet pair of points encompass all operators listed in Sec. III and are also shown in the previous Fig. 10. The blue points result from the simulation that excludes the diquark-antidiquark operator.

E. Outlook

This paper explores doubly heavy tetraquarks by analyzing their finite-volume energy spectrum using diquark-antidiquark operators at two different heavy quark masses. It addresses the left-hand cut in the DD^* scattering amplitude with the use of an effective potential evaluated in the plane-wave basis. However, this approach represents only one out of several that have been developed recently to deal with these issues.

One could employ the relativistic version of combined EFT and plane-wave approach [15,18], besides the nonrelativistic version that was used here due to the proximity of considered lattice energies to the DD^* threshold.

Various alternative ways of dealing with the left-hand cuts in scattering amplitudes have been proposed. For example, in Ref. [48] the two-particle Lüscher's formalism is generalized to explicitly account for the left-hand cut by relaxing some requirements of the original quantization condition, while more recently this has been extended to coupled channels and arbitrary spin in [49]. Reference [50] proposed a modified quantization condition in the presence of long-range forces that usually arise due to exchanges of light particles, such as one-pion exchange explicitly treated in this work, while Ref. [51] provides another strategy to deal with these challenges. In addition to these, Refs. [52,53] develop and apply to the T_{cc}, respectively, the 3-body quantization condition that effectively extends its range of validity all the way up to the first 4-particle states that can go on shell in a given channel. In this formalism D^* features as $D\pi$ bound state when $m_\pi > m_{D^*} - m_D$.

Another interesting possibility for a future study would be applying approach used here to investigate the pole trajectory of doubly charmed tetraquark as a function of light and heavy quark masses. This was touched upon in this paper and examined in our previous paper [7], albeit without the diquark-antidiquark operator in the basis. Dependence of the T_{cc} pole on the masses of the constituent quarks was analyzed also in [46,47].

The present one-channel study could also benefit from the extension to the coupled-channel $DD^* - D^*D^*$. This has been recently done in [8] at $m_\pi \simeq 390$ MeV with an expanded operator basis. Therein the authors apply Lüscher's quantization condition to lattice energies that are above the left-hand cut located below DD^* threshold.

In [12] a novel method of implementing diquark-antidiquark operators is proposed that is based on position-space sampling, thereby circumventing computational costs that arise naturally within distillation, as explained in more detail in Sec. IV, already at a relatively modest number of Laplacian eigenvectors. This method could be used in future simulations involving the diquark-antidiquark operator.

VIII. CONCLUSIONS

This work presented lattice QCD results on doubly heavy tetraquarks $QQ\bar{u}\,\bar{d}$ with $J^P = 1^+$ and $I = 0$ for $m_\pi \simeq 280$ MeV and heavy quark Q with charm or close to bottom quark mass.

Building upon the already existing meson-meson bilocal interpolators, we implemented additional localized diquark-antidiquark interpolators with the distillation method and explored their effects. We find that for $Q = c$ the diquark-antidiquark operator has a somewhat small $1 - 2\sigma$ effect on certain eigenenergies, the scattering amplitude, and the resulting pole location within our simulation framework. For $Q \simeq b$, the BB^* scattering operators alone do not render a deeply bound T_{bb}, and the inclusion of diquark-antidiquark operators is required, which shifts the ground state energy significantly down while also influencing other energy levels.

Our study presents the first extraction of DD^* scattering amplitude based on meson-meson as well as diquark antidiquark operators. The scattering amplitude was extracted from lattice eigenenergies in a framework combining an effective field theory and plane-wave approach. This framework is applicable also for energies on the left-hand cut, which is present in the lattice kinematics with stable D^*. Three low-energy constants of the EFT potential were fitted from nine lattice energies leading to a favorable reproduction of the lattice data. The resulting scattering amplitude agrees with the one obtained with the Lüscher's approach in the energy region above the left-hand cut where the latter is applicable.

The T_{cc} is found as a subthreshold resonance corresponding to a pole at $m_{T_{cc}} - m_D - m_{D^*} = -5.2^{+0.7}_{-0.8} - i \cdot 6.3^{+2.4}_{-4.8}$ MeV at the employed $m_\pi \simeq 280$ MeV. The presence of the pole near threshold results from a significant

attractive interaction between D and D^*. A small shift of the pole away from the real axes can be traced back to a slightly repulsive part of the one-pion exchange interaction at larger distances in our kinematics where $m_\pi > m_{D^*} - m_D$. Note that in the LHCb experiment, the T_{cc} pole is away from the real axes due to the three-body decay $DD\pi$, which is kinematically closed in our simulation as well as for all other existing lattice simulations.

Our code implementing distillation is written within the framework of the Chroma software package [54] and utilizes the Eigen library [55].

ACKNOWLEDGMENTS

We would like to thank V. Baru, S. Dawid, E. Epelbaum, L. Meng, A. Nefediev, F. Romero-López, and S. Sharpe for illuminating discussions. We thank our colleagues in CLS for the joint effort in the generation of the gauge field ensembles which form a basis for the computation. We use the multigrid solver of Refs. [56–59] for the inversion of the Dirac operator. The authors gratefully acknowledge the HPC RIVR consortium [60] and EuroHPC JU [61] for funding this research by providing computing resources of the HPC system Vega at the Institute of Information Science [62]. M. P. acknowledges the use of computing clusters at IMSc Chennai. We thank the authors of Ref. [63] for making the *TwoHadronsInBox* package public. The work of I. V., S. P., and L. L. is supported by the Slovenian Research Agency (research core Funding No. P1-0035, No. J1-3034 and No. N1-0360). M. P. gratefully acknowledges support from the Department of Science and Technology, India, SERB Start-up Research Grant No. SRG/2023/001235 and Department of Atomic Energy, India.

DATA AVAILABILITY

The data that support the findings of this article are openly available [64], embargo periods may apply.

APPENDIX A: VARIATION OF CUTOFF

The DD^* scattering amplitude in the main text is based on the effective field theory with our preferred values of the cutoff $\Lambda = 0.65$ GeV and rather a sharp fall-off in the regulator $f_{\rm reg}$ for the potential (22) and (23) obtained using $n = 40$. Such a cutoff is slightly above the noninteracting level $D(1)D^*(-1)$ on our smaller volume.

This appendix presents the fits to lattice eigen-energies (Figs. 12 and 14), the corresponding $p\cot\delta_0$ (Figs. 13 and 15) and pole positions (Fig. 16) also for a smoother regulator $n = 10$ and lower cutoff $\Lambda = 0.5$ GeV. The reproduction of certain lattice energies and resulting χ^2 is less favorable, however, the main conclusions based on all these choices remain robust: (i) the inclusion of diquark-antidiquark operators somewhat decreases $p\cot\delta_0$ and moves the T_{cc} pole slightly closer to the DD^* threshold, (ii) the resulting $p\cot\delta_0$ based on EFT and Lüscher's approach show reasonable agreement in the region above the left-hand cut, and (iii) the T_{cc} is a subthreshold resonance with a pole within 10 MeV of the threshold for all cases considered.

APPENDIX B: EXAMPLE OF THE PLANE-WAVE APPROACH FOR IRREP T_1^+

This appendix presents a simple application of the plane-wave formalism to the system consisting of a pseudoscalar meson (P) and a vector meson (V). For simplicity, we illustrate the irreducible representation T_1^+ of the 48-element Octahedral group O_h for total momentum zero, $\vec{P} = \vec{0}$. In the case of a sharp cutoff on the cmf momentum in the range $\Lambda = \frac{2\pi}{L} - \sqrt{2}\frac{2\pi}{L}$, the largest momentum shell of plane-waves that contributes to the total basis is $|\vec{p}| = \frac{2\pi}{L}$. Note that this also applies to the channel $PV = DD^*$ considered in the main body of this text with $\Lambda = 0.65$ GeV in the case of a sharp regulator f_{rep} in (23).

The relevant plane-wave basis $|P(\vec{k})V(-\vec{k},\vec{\epsilon}^{\,r})\rangle$ (25) is $(1+6)\times 3 = 21$-dimensional

$$\begin{pmatrix}
P(\vec{0})V_x(\vec{0}) \\
P(\vec{e}_x)V_x(-\vec{e}_x) \\
P(\vec{e}_y)V_x(-\vec{e}_y) \\
P(\vec{e}_z)V_x(-\vec{e}_z) \\
P(-\vec{e}_x)V_x(\vec{e}_x) \\
P(-\vec{e}_y)V_x(\vec{e}_y) \\
P(-\vec{e}_z)V_x(\vec{e}_z) \\
P(\vec{0})V_y(\vec{0}) \\
P(\vec{e}_x)V_y(-\vec{e}_x) \\
P(\vec{e}_y)V_y(-\vec{e}_y) \\
P(\vec{e}_z)V_y(-\vec{e}_z) \\
P(-\vec{e}_x)V_y(\vec{e}_x) \\
P(-\vec{e}_y)V_y(\vec{e}_y) \\
P(-\vec{e}_z)V_y(\vec{e}_z) \\
P(\vec{0})V_z(\vec{0}) \\
P(\vec{e}_x)V_z(-\vec{e}_x) \\
P(\vec{e}_y)V_z(-\vec{e}_y) \\
P(\vec{e}_z)V_z(-\vec{e}_z) \\
P(-\vec{e}_x)V_z(\vec{e}_x) \\
P(-\vec{e}_y)V_z(\vec{e}_y) \\
P(-\vec{e}_z)V_z(\vec{e}_z)
\end{pmatrix}. \tag{B1}$$

The representations of the kinetic energy operator $W_{\rm kin} = p^2/2m_r$ and the contact potential V_{CT} (22) in this basis form 21×21 matrices

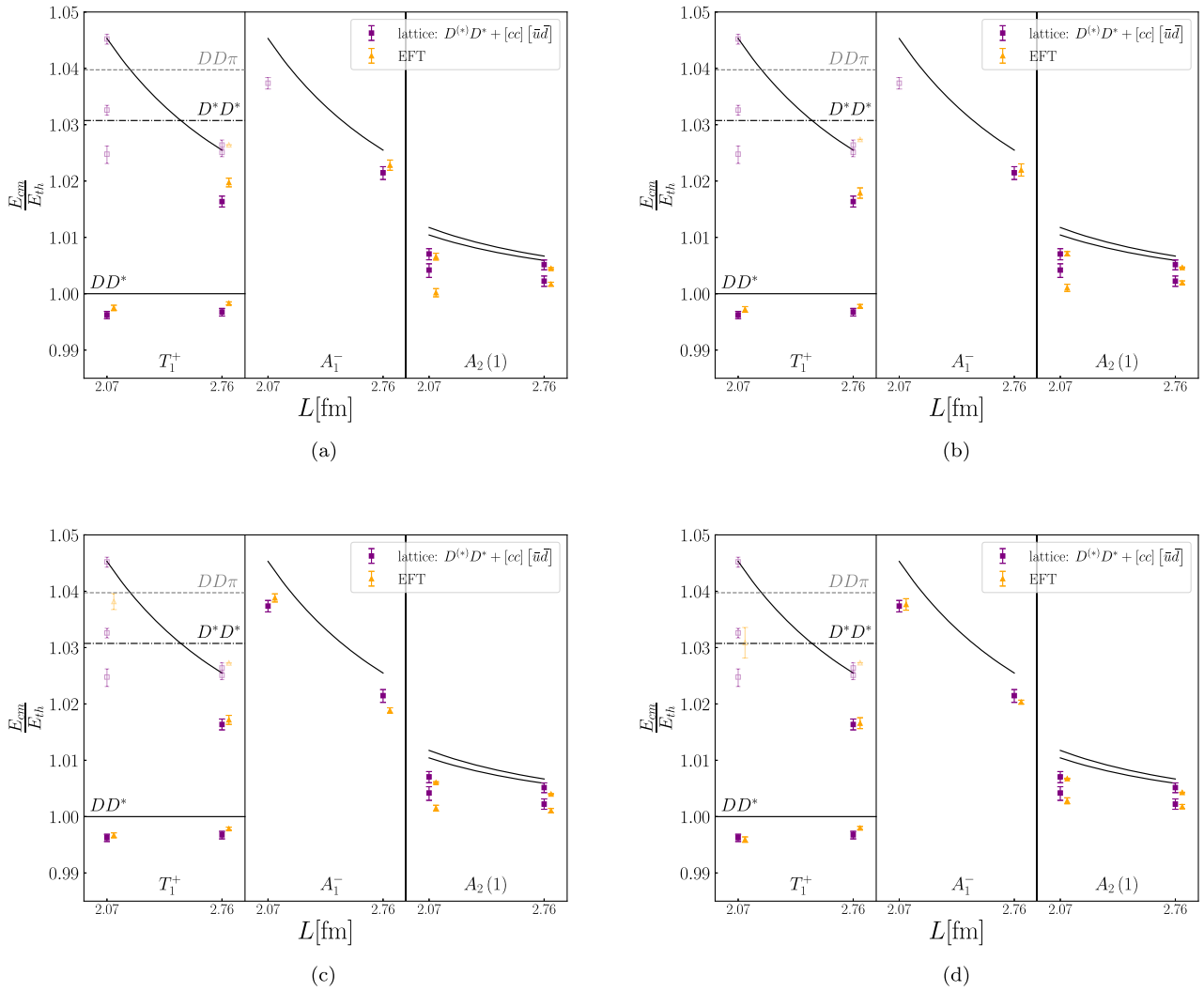

FIG. 12. Fit of the low-energy constants for various cutoffs Λ and shapes n in the regulator f_{reg} (23) of the potential: violet points represent lattice energies obtained with all interpolators, while orange points are the energies reconstructed from the fitted effective potential. (a) $\Lambda = 0.5\,\text{GeV}$, $n = 10, \frac{\chi^2}{n_{\text{d.o.f.}}} = 6.8$. (b) $\Lambda = 0.5\,\text{GeV}$, $n = 40, \frac{\chi^2}{n_{\text{d.o.f.}}} = 3.2$. (c) $\Lambda = 0.65\,\text{GeV}$, $n = 10, \frac{\chi^2}{n_{\text{d.o.f.}}} = 4.1$. (d) $\Lambda = 0.65\,\text{GeV}$, $n = 40, \frac{\chi^2}{n_{\text{d.o.f.}}} = 1.3$.

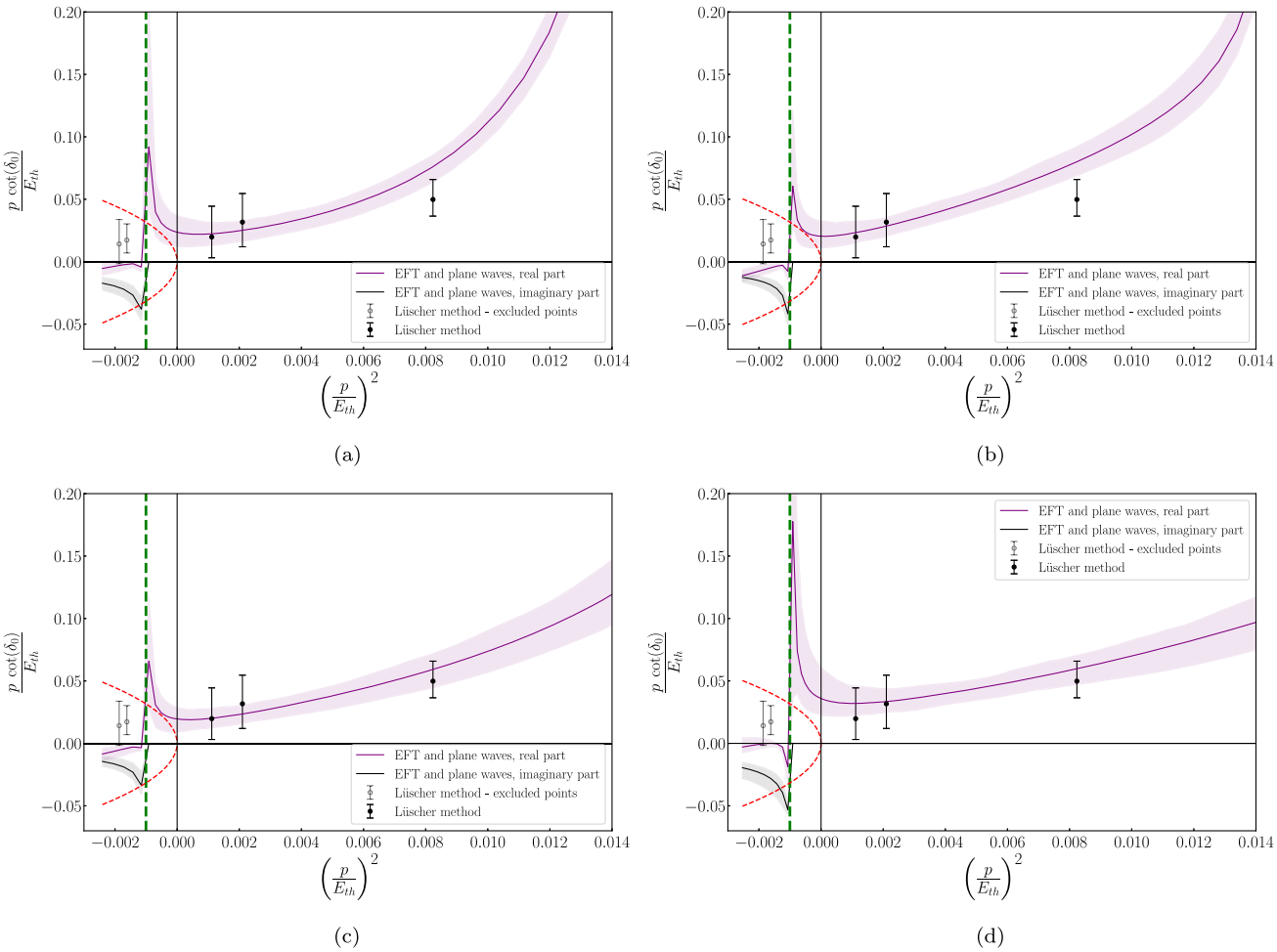

FIG. 13. $p\cot(\delta_0)$ for DD^* scattering obtained using all interpolators. Violet curve: The result is based on an EFT fit to lattice energies (with given χ^2) for various Λ and n in the potential regulator $f_{\rm reg}$ (23). Black circles: results based on Lüscher's approach which is applicable only above the left-hand cut shown by the green dashed line. (a) $\Lambda = 0.5\,\mathrm{GeV}$, $n = 10, \frac{\chi^2}{n_{\rm d.o.f.}} = 6.8$. (b) $\Lambda = 0.5\,\mathrm{GeV}$, $n = 40, \frac{\chi^2}{n_{\rm d.o.f.}} = 3.2$. (c) $\Lambda = 0.65\,\mathrm{GeV}$, $n = 10, \frac{\chi^2}{n_{\rm d.o.f.}} = 4.1$. (d) $\Lambda = 0.65\,\mathrm{GeV}$, $n = 40, \frac{\chi^2}{n_{\rm d.o.f.}} = 1.3$.

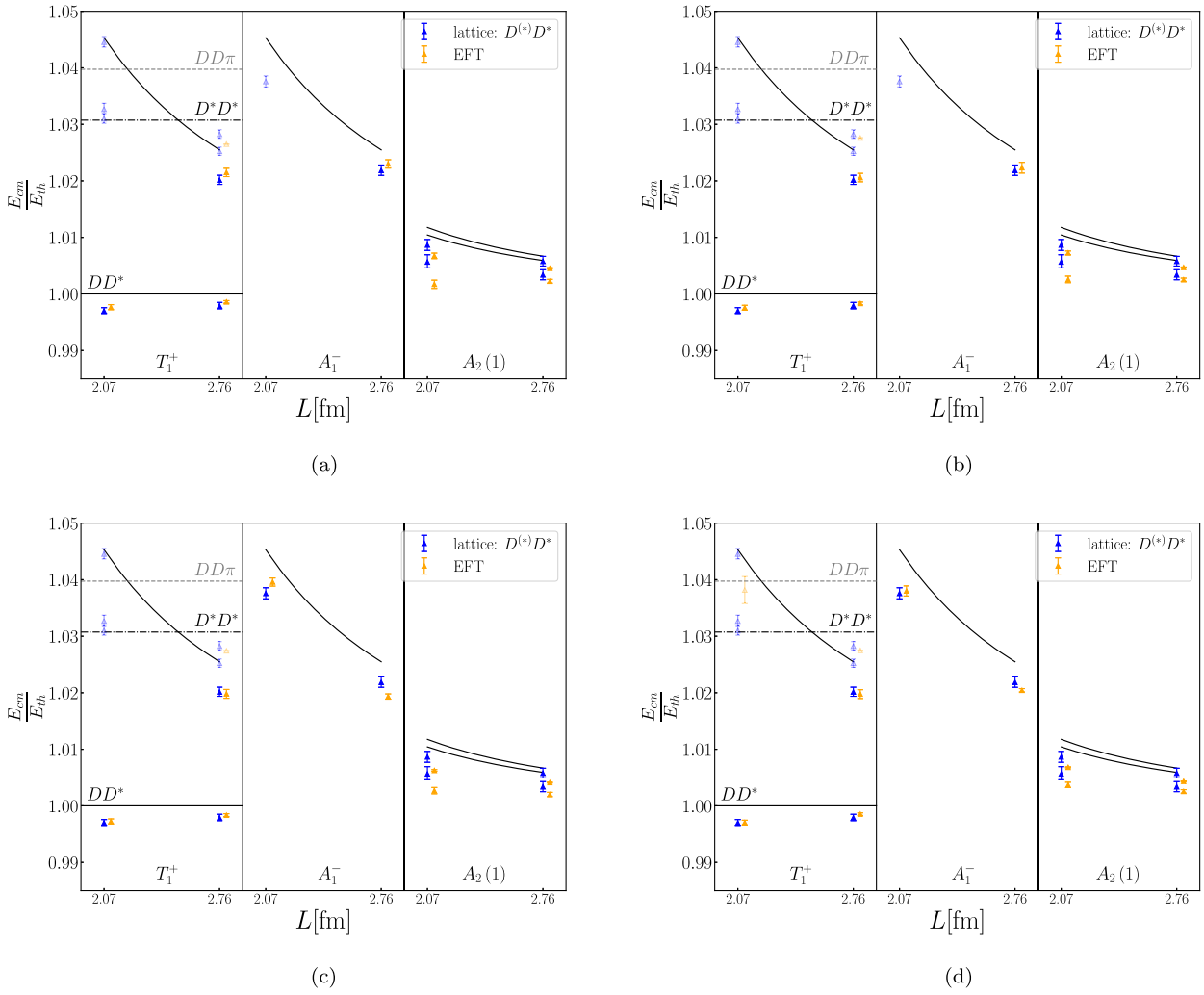

FIG. 14. Same as Fig. 12, but for lattice data based solely on meson-meson operators. (a) $\Lambda = 0.5\,\mathrm{GeV}$, $n = 10, \frac{\chi^2}{n_{\mathrm{d.o.f.}}} = 5.4$. (b) $\Lambda = 0.5\,\mathrm{GeV}$, $n = 40, \frac{\chi^2}{n_{\mathrm{d.o.f.}}} = 2.8$. (c) $\Lambda = 0.65\,\mathrm{GeV}$, $n = 10, \frac{\chi^2}{n_{\mathrm{d.o.f.}}} = 5.5$. (d) $\Lambda = 0.65\,\mathrm{GeV}$, $n = 40, \frac{\chi^2}{n_{\mathrm{d.o.f.}}} = 2.4$.

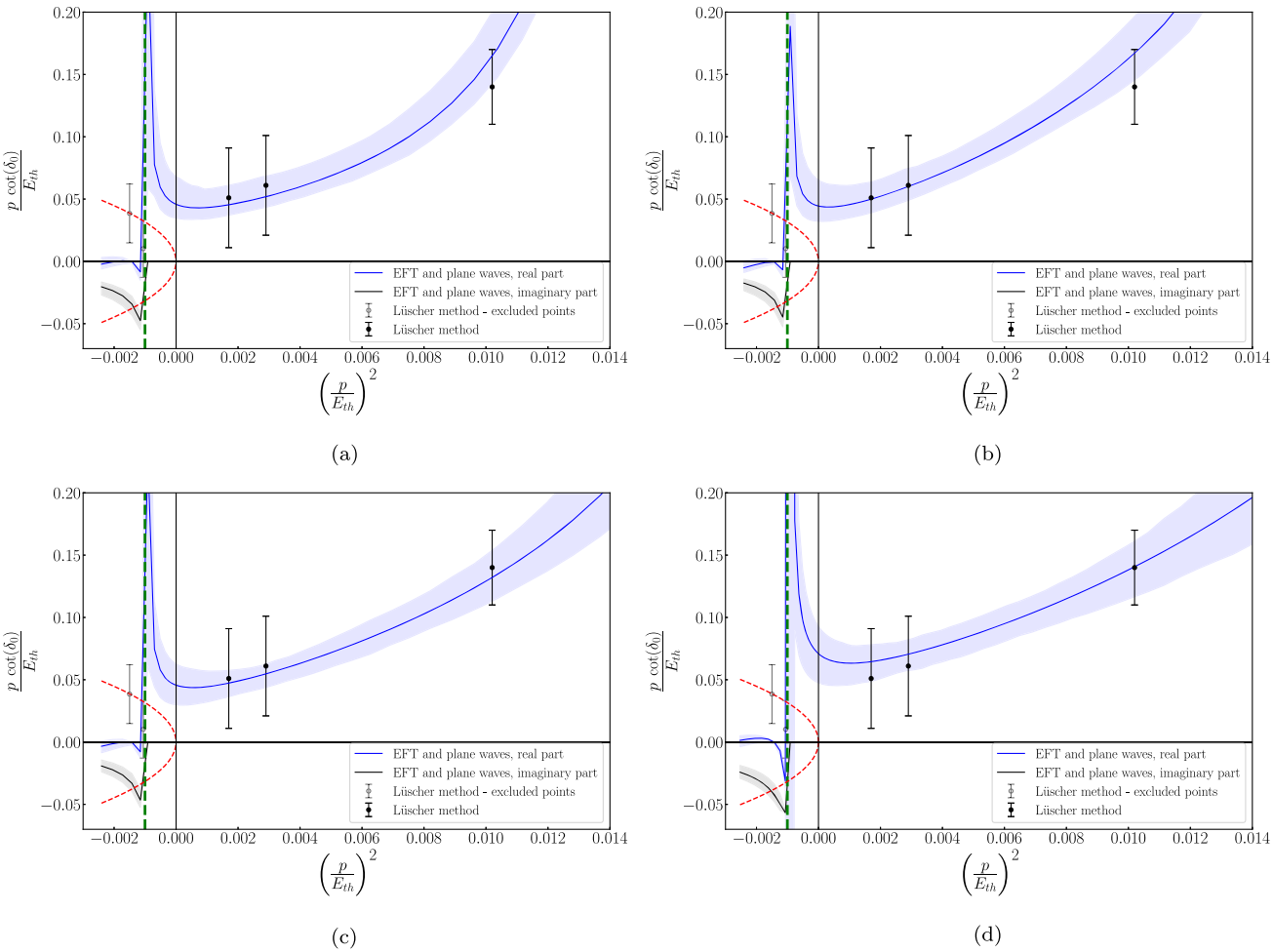

FIG. 15. Same as Fig. 13, but for lattice data based solely on meson-meson operators. (a) $\Lambda = 0.5\,\mathrm{GeV}$, $n = 10, \frac{\chi^2}{n_{\mathrm{d.o.f.}}} = 5.4$. (b) $\Lambda = 0.5\,\mathrm{GeV}$, $n = 40, \frac{\chi^2}{n_{\mathrm{d.o.f.}}} = 2.8$. (c) $\Lambda = 0.65\,\mathrm{GeV}$, $n = 10, \frac{\chi^2}{n_{\mathrm{d.o.f.}}} = 5.5$. (d) $\Lambda = 0.65\,\mathrm{GeV}$, $n = 40, \frac{\chi^2}{n_{\mathrm{d.o.f.}}} = 2.4$.

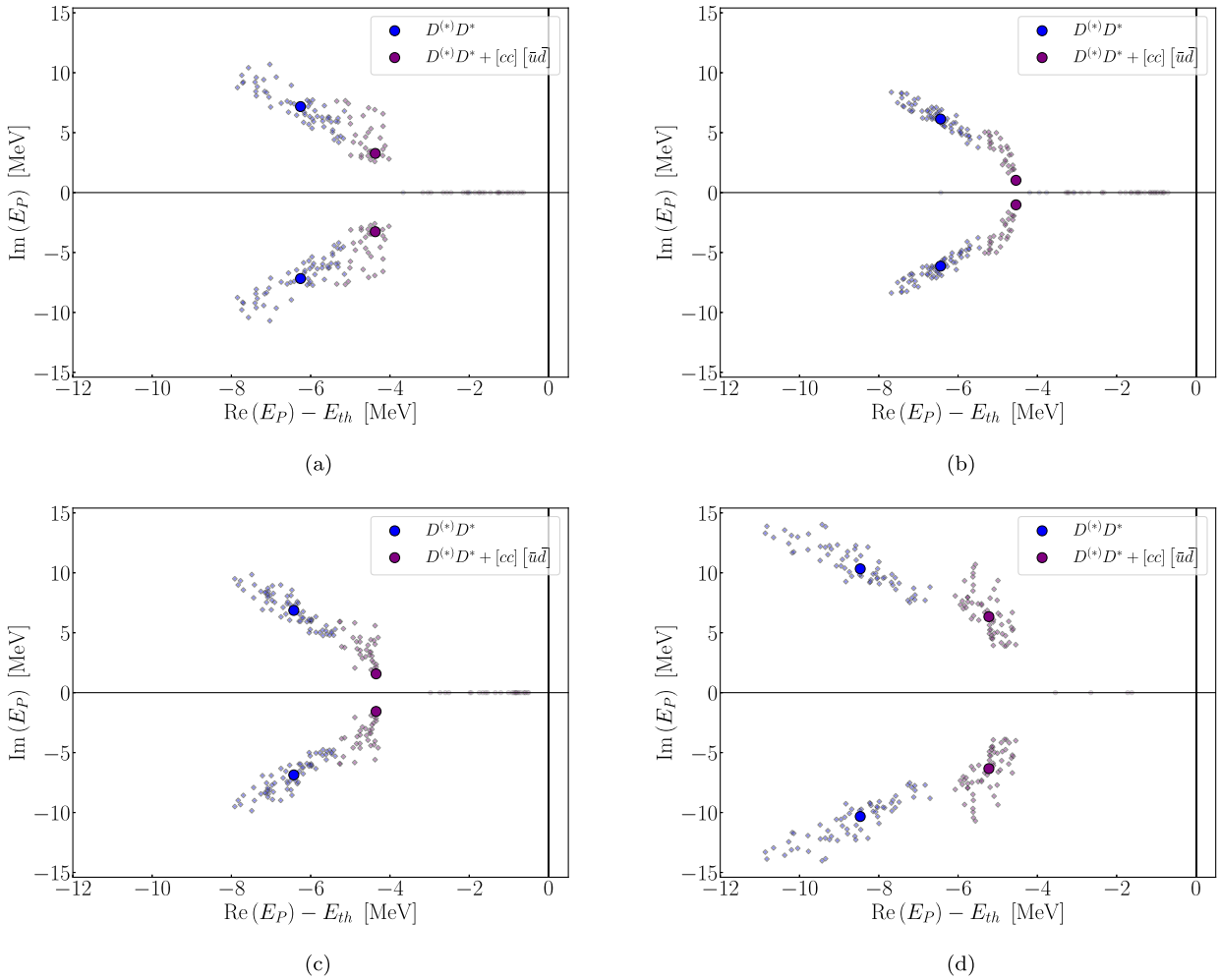

FIG. 16. Location of the T_{cc}^+ pole obtained from our lattice results including (violet) or excluding (blue) diquark antidiquark operators. The results based on various cutoffs Λ and n in the potential regulator f_{reg} (23) are shown. The large circle represents the central value, while the distribution of the small diamonds represents the 1σ error band. More precisely, the dispersed points shown are generated from a hundred pseudorandom samples of the low-energy constants that are normally distributed according to their central values and the covariance matrix obtained from the fit to the lattice spectrum, as explained in Sec. VII A. Each of these points is calculated by taking one such sample and solving the LSE (11). The points outside of 1σ range of central values are not shown. The origin represents the DD^* threshold. (a) $\Lambda = 0.5\,\mathrm{GeV}$, $n = 10, \frac{\chi^2}{n_{\mathrm{d.o.f.}}} = 6.8, \frac{\chi^2}{n_{\mathrm{d.o.f.}}} = 5.4$. (b) $\Lambda = 0.5\,\mathrm{GeV}$, $n = 40, \frac{\chi^2}{n_{\mathrm{d.o.f.}}} = 3.2, \frac{\chi^2}{n_{\mathrm{d.o.f.}}} = 2.8$. (c) $\Lambda = 0.65\,\mathrm{GeV}$, $n = 10, \frac{\chi^2}{n_{\mathrm{d.o.f.}}} = 4.1, \frac{\chi^2}{n_{\mathrm{d.o.f.}}} = 5.5$. (d) $\Lambda = 0.65\,\mathrm{GeV}$, $n = 40, \frac{\chi^2}{n_{\mathrm{d.o.f.}}} = 1.3, \frac{\chi^2}{n_{\mathrm{d.o.f.}}} = 2.4$.

$$W_{\rm kin} = \begin{pmatrix} w_{\rm kin} & 0 & 0 \\ 0 & w_{\rm kin} & 0 \\ 0 & 0 & w_{\rm kin} \end{pmatrix}, \quad V_{CT} = \begin{pmatrix} v_{CT} & 0 & 0 \\ 0 & v_{CT} & 0 \\ 0 & 0 & v_{CT} \end{pmatrix},$$

$$w_{\rm kin} = \frac{1}{2m_r}\begin{pmatrix} 0 & 0 & 0 & 0 & 0 & 0 & 0 \\ 0 & \left(\frac{2\pi}{L}\right)^2 & 0 & 0 & 0 & 0 & 0 \\ 0 & 0 & \left(\frac{2\pi}{L}\right)^2 & 0 & 0 & 0 & 0 \\ 0 & 0 & 0 & \left(\frac{2\pi}{L}\right)^2 & 0 & 0 & 0 \\ 0 & 0 & 0 & 0 & \left(\frac{2\pi}{L}\right)^2 & 0 & 0 \\ 0 & 0 & 0 & 0 & 0 & \left(\frac{2\pi}{L}\right)^2 & 0 \\ 0 & 0 & 0 & 0 & 0 & 0 & \left(\frac{2\pi}{L}\right)^2 \end{pmatrix},$$

$$v_{CT} = \begin{pmatrix} c_0 & c_0+c_2 & c_0+c_2 & c_0+c_2 & c_0+c_2 & c_0+c_2 & c_0+c_2 \\ c_0+c_2 & c_0+2c_2 & c_0+2c_2 & c_0+2c_2 & c_0+2c_2 & c_0+2c_2 & c_0+2c_2 \\ c_0+c_2 & c_0+2c_2 & c_0+2c_2 & c_0+2c_2 & c_0+2c_2 & c_0+2c_2 & c_0+2c_2 \\ c_0+c_2 & c_0+2c_2 & c_0+2c_2 & c_0+2c_2 & c_0+2c_2 & c_0+2c_2 & c_0+2c_2 \\ c_0+c_2 & c_0+2c_2 & c_0+2c_2 & c_0+2c_2 & c_0+2c_2 & c_0+2c_2 & c_0+2c_2 \\ c_0+c_2 & c_0+2c_2 & c_0+2c_2 & c_0+2c_2 & c_0+2c_2 & c_0+2c_2 & c_0+2c_2 \\ c_0+c_2 & c_0+2c_2 & c_0+2c_2 & c_0+2c_2 & c_0+2c_2 & c_0+2c_2 & c_0+2c_2 \end{pmatrix}, \quad c_0 \equiv c_0^s, \quad c_2 \equiv c_2^s\left(\frac{2\pi}{L}\right)^2. \quad \text{(B2)}$$

Note that the p-wave contribution in (B2), proportional to the low-energy constant c_2^p, is omitted since its projection to the considered T_1^+ irrep vanishes.

General relations required to project the Hamiltonian $H = W_{\rm kin} + V_{CT}$ to arbitrary irreducible representations Γ are presented in Eqs. (3.5)–(3.10) of [18]. To this end, we utilize the matrix $U^{T_{1z}^+}$ that contains the maximally linearly independent set of orthonormal vectors which transform according to the T_1^+ irrep. Due to rotational invariance, it suffices to consider only a single row of the irrep, e.g., the z-component. The full projection of the 21-dimensional plane-wave basis (B1) to the basis that transforms accordingly is then encoded by the 3×21 unitary matrix

$$U^{T_{1z}^+} = \begin{pmatrix} u_x & u_y & u_z \end{pmatrix}, \qquad u_z = \begin{pmatrix} 1 & 0 & 0 & 0 & 0 & 0 & 0 \\ 0 & 0 & 0 & \frac{1}{\sqrt{2}} & 0 & 0 & \frac{1}{\sqrt{2}} \\ 0 & \frac{1}{2} & \frac{1}{2} & 0 & \frac{1}{2} & \frac{1}{2} & 0 \end{pmatrix},$$

$$u_{x,y} = \begin{pmatrix} 0 & 0 & 0 & 0 & 0 & 0 & 0 \\ 0 & 0 & 0 & 0 & 0 & 0 & 0 \\ 0 & 0 & 0 & 0 & 0 & 0 & 0 \end{pmatrix}. \quad \text{(B3)}$$

The Hamiltonian, projected to T_{1z}^+, is defined as $H^{T_1^+} = U^{T_{1z}^+} H (U^{T_{1z}^+})^\dagger$ and its eigenvalues are fitted to the lattice energies according to (17). In the absence of one-pion exchange and with definitions in (B2), this Hamiltonian then evaluates to

$$H^{T_1^+} = U^{T_{1z}^+}(W_{\text{kin}} + V_{CT})(U^{T_{1z}^+})^\dagger = \begin{pmatrix} c_0 & \sqrt{2}(c_0+c_2) & 2(c_0+c_2) \\ \sqrt{2}(c_0+c_2) & 2c_0+4c_2+\left(\frac{2\pi}{L}\right)^2 & 2\sqrt{2}(c_0+2c_2) \\ 2(c_0+c_2) & 2\sqrt{2}(c_0+2c_2) & 4c_0+8c_2+\left(\frac{2\pi}{L}\right)^2 \end{pmatrix}. \tag{B4}$$

[1] R. Aaij *et al.* (LHCb Collaboration), Observation of an exotic narrow doubly charmed tetraquark, Nat. Phys. **18**, 751 (2022).

[2] R. Aaij *et al.* (LHCb Collaboration), Study of the doubly charmed tetraquark T_{cc}^+, Nat. Commun. **13**, 3351 (2022).

[3] L. Meng, E. Ortiz-Pacheco, V. Baru, E. Epelbaum, M. Padmanath, and S. Prelovsek, Doubly charm tetraquark channel with isospin 1 from lattice QCD, Phys. Rev. D **111**, 034509 (2025).

[4] M. Padmanath and S. Prelovsek, Signature of a doubly charm tetraquark pole in DD* scattering on the lattice, Phys. Rev. Lett. **129**, 032002 (2022).

[5] S. Chen, C. Shi, Y. Chen, M. Gong, Z. Liu, W. Sun, and R. Zhang, $T_{cc}^+(3875)$ relevant DD* scattering from $N_f = 2$ lattice QCD, Phys. Lett. B **833**, 137391 (2022).

[6] Y. Lyu, S. Aoki, T. Doi, T. Hatsuda, Y. Ikeda, and J. Meng, Doubly charmed tetraquark T_{cc}^+ from lattice QCD near physical point, Phys. Rev. Lett. **131**, 161901 (2023).

[7] S. Collins, A. Nefediev, M. Padmanath, and S. Prelovsek, Toward the quark mass dependence of T_{cc}^+ from lattice QCD, Phys. Rev. D **109**, 094509 (2024).

[8] T. Whyte, D. J. Wilson, and C. E. Thomas (Hadron Spectrum Collaboration), Near-threshold states in coupled DD*-D*D* scattering from lattice QCD, Phys. Rev. D **111**, 034511 (2025).

[9] G. K. C. Cheung, C. E. Thomas, J. J. Dudek, and R. G. Edwards (Hadron Spectrum Collaboration), Tetraquark operators in lattice QCD and exotic flavour states in the charm sector, J. High Energy Phys. 11 (2017) 033.

[10] P. Junnarkar, N. Mathur, and M. Padmanath, Study of doubly heavy tetraquarks in lattice QCD, Phys. Rev. D **99**, 034507 (2019).

[11] E. Ortiz-Pacheco, S. Collins, L. Leskovec, M. Padmanath, and S. Prelovsek, Doubly charmed tetraquark: Isospin channels and diquark-antidiquark interpolators, Proc. Sci. LATTICE2023 (**2024**) 052 [arXiv:2312.13441].

[12] A. Stump and J. R. Green, Distillation and position-space sampling for local multiquark interpolators, Proc. Sci. LATTICE2024 (**2025**) 094 [arXiv:2412.09246].

[13] I. Vujmilovic, S. Collins, L. Leskovec, E. Ortiz-Pacheco, M. Padmanath, and S. Prelovsek, T_{cc}^+ via the plane wave approach and including diquark-antidiquark operators, Proc. Sci. LATTICE2024 (**2025**) 112 [arXiv:2411.08646].

[14] M.-L. Du, A. Filin, V. Baru, X.-K. Dong, E. Epelbaum, F.-K. Guo, C. Hanhart, A. Nefediev, J. Nieves, and Q. Wang, Role of left-hand cut contributions on pole extractions from lattice data: Case study for $T_{cc}^+(3875)$, Phys. Rev. Lett. **131**, 131903 (2023).

[15] L. Meng, V. Baru, E. Epelbaum, A. A. Filin, and A. M. Gasparyan, Solving the left-hand cut problem in lattice QCD: $T_{cc}^+(3875)$ from finite volume energy levels, Phys. Rev. D **109**, L071506 (2024).

[16] M. Luscher, Volume dependence of the energy spectrum in massive quantum field theories. 2. Scattering states, Commun. Math. Phys. **105**, 153 (1986).

[17] R. A. Briceno, J. J. Dudek, and R. D. Young, Scattering processes and resonances from lattice QCD, Rev. Mod. Phys. **90**, 025001 (2018).

[18] L. Meng and E. Epelbaum, Two-particle scattering from finite-volume quantization conditions using the plane wave basis, J. High Energy Phys. 10 (2021) 051.

[19] A. Francis, R. J. Hudspith, R. Lewis, and K. Maltman, Lattice prediction for deeply bound doubly heavy tetraquarks, Phys. Rev. Lett. **118**, 142001 (2017).

[20] L. Leskovec, S. Meinel, M. Pflaumer, and M. Wagner, Lattice QCD investigation of a doubly-bottom $\bar{b}\bar{b}ud$ tetraquark with quantum numbers $I(J^P) = 0(1^+)$, Phys. Rev. D **100**, 014503 (2019).

[21] C. Alexandrou, J. Finkenrath, T. Leontiou, S. Meinel, M. Pflaumer, and M. Wagner, bb ud and bb us tetraquarks from lattice QCD using symmetric correlation matrices with both local and scattering interpolating operators, Phys. Rev. D **110**, 054510 (2024).

[22] B. Colquhoun, A. Francis, R. J. Hudspith, R. Lewis, K. Maltman, and W. G. Parrott, Improved analysis of strong-interaction-stable doubly bottom tetraquarks on the lattice, Phys. Rev. D **110**, 094503 (2024).

[23] B. S. Tripathy, N. Mathur, and M. Padmanath, $bb\bar{u}\bar{d}$ and $bs\bar{u}\bar{d}$ tetraquarks from lattice QCD using two-meson and diquark-antidiquark variational basis, Phys. Rev. D **111**, 114504 (2025).

[24] M. Bruno *et al.*, Simulation of QCD with $N_f = 2 + 1$ flavors of non-perturbatively improved Wilson fermions, J. High Energy Phys. 02 (2015) 043.

[25] G. S. Bali, E. E. Scholz, J. Simeth, and W. Söldner (RQCD Collaboration), Lattice simulations with $N_f = 2 + 1$

improved Wilson fermions at a fixed strange quark mass, Phys. Rev. D **94**, 074501 (2016).
[26] M. Bruno, T. Korzec, and S. Schaefer, Setting the scale for the CLS 2 + 1 flavor ensembles, Phys. Rev. D **95**, 074504 (2017).
[27] S. Prelovsek, S. Collins, D. Mohler, M. Padmanath, and S. Piemonte, Charmonium-like resonances with $J^{PC} = 0^{++}$, 2^{++} in coupled $D\bar{D}$, $D_s\bar{D}_s$ scattering on the lattice, J. High Energy Phys. 06 (2021) 035.
[28] M. Luscher and U. Wolff, How to calculate the elastic scattering matrix in two-dimensional quantum field theories by numerical simulation, Nucl. Phys. **B339**, 222 (1990).
[29] B. Blossier, M. Della Morte, G. von Hippel, T. Mendes, and R. Sommer, On the generalized eigenvalue method for energies and matrix elements in lattice field theory, J. High Energy Phys. 04 (2009) 094.
[30] R. L. Jaffe, Exotica, Phys. Rep. **409**, 1 (2005).
[31] M. Peardon, J. Bulava, J. Foley, C. Morningstar, J. Dudek, R. G. Edwards, B. Joo, H.-W. Lin, D. G. Richards, and K. J. Juge (Hadron Spectrum Collaboration), A novel quark-field creation operator construction for hadronic physics in lattice QCD, Phys. Rev. D **80**, 054506 (2009).
[32] M. Padmanath, S. Collins, D. Mohler, S. Piemonte, S. Prelovsek, A. Schäfer, and S. Weishaeupl, Identifying spin and parity of charmonia in flight with lattice QCD, Phys. Rev. D **99**, 014513 (2019).
[33] S. Piemonte, S. Collins, D. Mohler, M. Padmanath, and S. Prelovsek, Charmonium resonances with $J^{PC} = 1^{--}$ and 3^{--} from $\bar{D}D$ scattering on the lattice, Phys. Rev. D **100**, 074505 (2019).
[34] J. F. Nieves and P. B. Pal, Generalized Fierz identities, Am. J. Phys. **72**, 1100 (2004).
[35] M. Padmanath, C. B. Lang, and S. Prelovsek, X(3872) and Y(4140) using diquark-antidiquark operators with lattice QCD, Phys. Rev. D **92**, 034501 (2015).
[36] P. Bicudo and M. Wagner (European Twisted Mass Collaboration), Lattice QCD signal for a bottom-bottom tetraquark, Phys. Rev. D **87**, 114511 (2013).
[37] P. Bicudo, K. Cichy, A. Peters, and M. Wagner, BB interactions with static bottom quarks from lattice QCD, Phys. Rev. D **93**, 034501 (2016).
[38] M. Karliner and J. L. Rosner, Discovery of doubly-charmed Ξ_{cc} baryon implies a stable $(bb\bar{u}\,\bar{d})$ tetraquark, Phys. Rev. Lett. **119**, 202001 (2017).
[39] D. Janc and M. Rosina, The $T_{cc} = DD^*$ molecular state, Few-Body Syst. **35**, 175 (2004).
[40] P. Mohanta and S. Basak, Construction of $bb\bar{u}\,\bar{d}$ tetraquark states on lattice with NRQCD bottom and HISQ up and down quarks, Phys. Rev. D **102**, 094516 (2020).
[41] R. J. Hudspith and D. Mohler, Exotic tetraquark states with two b quarks and $J^P = 0^+$ and $1^+ B_s$ states in a non-perturbatively tuned lattice NRQCD setup, Phys. Rev. D **107**, 114510 (2023).
[42] T. Aoki, S. Aoki, and T. Inoue, Lattice study on a tetraquark state T_{bb} in the HAL QCD method, Phys. Rev. D **108**, 054502 (2023).
[43] S. Fleming, M. Kusunoki, T. Mehen, and U. van Kolck, Pion interactions in the $X(3872)$, Phys. Rev. D **76**, 034006 (2007).
[44] D. Becirevic and F. Sanfilippo, Theoretical estimate of the $D^* \to D\pi$ decay rate, Phys. Lett. B **721**, 94 (2013).
[45] S. Prelovsek, U. Skerbis, and C. B. Lang, Lattice operators for scattering of particles with spin, J. High Energy Phys. 01 (2017) 129.
[46] F. Gil-Domínguez, A. Giachino, and R. Molina, Quark mass dependence of the $T_{cc}^+(3875)$ pole, Phys. Rev. D **111**, 016029 (2025).
[47] M. Abolnikov, V. Baru, E. Epelbaum, A. A. Filin, C. Hanhart, and L. Meng, Internal structure of the $T_{cc}^+(3875)$ from its light-quark mass dependence, Phys. Lett. B **860**, 139188 (2025).
[48] A. B. Raposo and M. T. Hansen, Finite-volume scattering on the left-hand cut, J. High Energy Phys. 08 (2024) 075.
[49] A. B. Raposo, R. A. Briceño, M. T. Hansen, and A. W. Jackura, Extracting scattering amplitudes for arbitrary two-particle systems with one-particle left-hand cuts via lattice QCD, arXiv:2502.19375.
[50] R. Bubna, H.-W. Hammer, F. Müller, J.-Y. Pang, A. Rusetsky, and J.-J. Wu, Lüscher equation with long-range forces, J. High Energy Phys. 05 (2024) 168.
[51] S. M. Dawid, A. W. Jackura, and A. P. Szczepaniak, Finite-volume quantization condition from the N/D representation, Phys. Lett. B **864**, 139442 (2025).
[52] M. T. Hansen and S. R. Sharpe, Relativistic, model-independent, three-particle quantization condition, Phys. Rev. D **90**, 116003 (2014).
[53] S. M. Dawid, F. Romero-López, and S. R. Sharpe, Finite- and infinite-volume study of DDπ scattering, J. High Energy Phys. 01 (2025) 060.
[54] R. G. Edwards and B. Joo (SciDAC, LHPC, and UKQCD Collaborations), The Chroma software system for lattice QCD, Nucl. Phys. B, Proc. Suppl. **140**, 832 (2005).
[55] G. Guennebaud, B. Jacob *et al.*, Eigen v3, http://eigen.tuxfamily.org (2010).
[56] S. Heybrock, B. Joó, D. D. Kalamkar, M. Smelyanskiy, K. Vaidyanathan, T. Wettig, and P. Dubey, Lattice QCD with domain decomposition on Intel Xeon Phi™ co-processors, in *The International Conference for High Performance Computing, Networking, Storage, and Analysis: SC14: HPC matters* (2014), 10.1109/SC.2014.11.
[57] S. Heybrock, M. Rottmann, P. Georg, and T. Wettig, Adaptive algebraic multigrid on SIMD architectures, Proc. Sci. LATTICE2015 (**2016**) 036 [arXiv:1512.04506].
[58] D. Richtmann, S. Heybrock, and T. Wettig, Multiple right-hand-side setup for the DD-αAMG, Proc. Sci. LATTICE2015 (**2016**) 035 [arXiv:1601.03184].
[59] P. Georg, D. Richtmann, and T. Wettig, pMR: A high-performance communication library, Proc. Sci. LATTICE2016 (**2017**) 361. [arXiv:1701.08521].
[60] https://www.hpc-rivr.si.
[61] https://eurohpc-ju.europa.eu/index_en.
[62] https://www.izum.si.
[63] C. Morningstar, J. Bulava, B. Singha, R. Brett, J. Fallica, A. Hanlon, and B. Hörz, Estimating the two-particle K-matrix for multiple partial waves and decay channels from finite-volume energies, Nucl. Phys. **B924**, 477 (2017).
[64] http://www-f1.ijs.si/sasa/available-lattice-data.html